AGU PUBLICATIONS

Journal of Advances in Modeling Earth Systems



RESEARCH ARTICLE

10.1002/2016MS000809

# Improved MJO-simulation in ECHAM6.3 by coupling a Stochastic Multicloud Model to the convection scheme

**Karsten Peters**[1,2], **Traute Crueger**[2], **Christian Jakob**[1], **and Benjamin Möbis**[1]

[1]ARC Centre of Excellence for Climate System Science, School of Earth, Atmosphere and Environment, Monash University, Clayton, Australia, [2]Max-Planck-Institut für Meteorologie, Hamburg, Germany

**Key Points:**
- An observations-informed version of the Stochastic Multicloud Model (SMCM) is coupled to ECHAM6.3
- The SMCM in ECHAM6.3 improves the simulation of tropical intraseasonal variability including the MJO
- Capturing the spatiotemporal coherence of tropical rainfall on daily timescales is key to MJO simulation

**Supporting Information:**
- Supporting Information S1

**Correspondence to:**
K. Peters,
karsten.peters@mpimet.mpg.de

**Citation:**
Peters, K., T. Crueger, C. Jakob, and B. Möbis (2017), Improved MJO-simulation in ECHAM6.3 by coupling a Stochastic Multicloud Model to the convection scheme, *J. Adv. Model. Earth Syst.*, *9*, 193–219, doi:10.1002/2016MS000809.

Received 19 SEP 2016
Accepted 12 DEC 2016
Accepted article online 27 DEC 2016
Published online 25 JAN 2017



**Abstract** We implement a Stochastic Multicloud Model (SMCM) in an observation-informed configuration into the convection scheme of the state-of-the-art GCM ECHAM6.3. The SMCM configuration we use here has been tuned to represent observed tropical convection by associating the occurrence and strength of deep convection to midtropospheric vertical velocity and relative humidity. We show that compared to the ECHAM6.3 standard model, the SMCM-modified version shows improved capacity to simulate features of tropical intraseasonal variability, including MJO-like disturbances, without significantly distorting the mean model climate. This improvement goes in hand with ameliorated coupling of atmospheric convection to tropospheric moisture and spatiotemporal coherence of tropical convection compared to reanalysis and observations. We attribute these effects to (i) improved coupling of triggering and suppression of deep convective events to the model's large-scale environment and (ii) the observations-informed closure formulation which leads to an overall reduction of deep convective mass fluxes. Sensitivity tests show that while (ii) improves the convection-moisture relationship, it is (i) which improves the spatiotemporal coherence of tropical rainfall and is important for MJO simulation. Further, the simulated spatiotemporal coherence of tropical rainfall is an intrinsic property of the convection schemes themselves and not of their parameters. We stress that this study serves as a proof-of-concept and motivates further efforts towards building a novel convection parameterization with the SMCM as a central element.

## 1. Introduction

Atmospheric moist convection is one of the largest sources of precipitation and clouds. It is also the key process for the vertical redistribution of heat and moisture. As such, atmospheric moist convection must be adequately represented in global climate models (GCMs). The still coarse horizontal grid spacings of current generation GCMs do not allow for explicitly resolving convective processes, implying that in most GCMs convection and its effect on the general circulation are represented by a subgrid conceptual model—the convection parameterization (or *convection scheme*). Despite decades of GCM development, atmospheric moist convection remains poorly represented in GCMs—especially in the low latitudes [*Randall et al.*, 2007; *Flato et al.*, 2013]. Most of these errors are thought as being related to shortcomings in the convection schemes employed in current generation GCMs [e.g., *Stevens and Bony*, 2013]. Thus, accelerating the understanding of atmospheric moist convection and its coupling to the general circulation to inform the development of improved convection schemes is of utmost importance for GCM development [*Jakob*, 2010; *Stevens and Bony*, 2013; *Jakob*, 2014; *Bony et al.*, 2015].

In this study, we present first steps taken toward the development of a novel convective parameterization based on the coupling of a version of the Stochastic Multicloud Model (SMCM) [*Khouider et al.*, 2010]—tuned by *Peters et al.* [2013] to represent observed tropical convection—to the convection scheme of the GCM ECHAM6.3 [*Stevens et al.*, 2013].

Observations show that a large portion of tropical precipitation and the associated atmospheric dynamics are characterized by a conglomerate of east and westward-propagating convective clusters, organized by so-called convectively coupled equatorial waves (CCEWs) and the Madden-Julian-Oscillation (MJO) [*Zhang*, 2005; *Kiladis et al.*, 2009]. The MJO is an important element of tropical intraseasonal variability (TISV) and the exact processes which determine its emergence and maintenance are still unclear and a number of observational and modeling efforts have recently been set up to facilitate "Cracking the MJO nut" [cf., *Zhang et al.*, 2013 for

a comprehensive list of initiatives]. Consequently, shortcomings of GCM-simulated precipitation feature prominently in the (mis)representation of TISV [e.g., *Sperber and Kim*, 2012; *Jiang et al*., 2015; *Klingaman et al*., 2015].

It is widely accepted that a GCM's capacity to provide an adequate simulation of TISV is to a large part determined by the employed convection scheme [*Zhang*, 2005]. Some approaches to tackle the lack of TISV in GCMs incorporate stochastic perturbations into essential parts of the convection scheme and find an improved simulation of TISV [*Lin and Neelin*, 2000, 2003; *Teixeira and Reynolds*, 2008]. Although appealing in their simplicity, such approaches do not help in identifying the more deeply rooted errors in convection schemes. One of such errors is that operational convection schemes often do not provide for a realistic atmospheric moisture-precipitation relationship [*Derbyshire et al*., 2004; *Del Genio*, 2012]. Making the simulation of tropical deep convection more sensitive to midtropospheric moisture indeed leads to improved simulation of the MJO and TISV [*Kim et al*., 2011, 2012; *Del Genio et al*., 2012; *Hirons et al*., 2013a; *Klingaman and Woolnough*, 2014; *Hannah and Maloney*, 2014; *Zhu and Hendon*, 2015]—doing so can degrade the overall simulation of tropical climate, though [e.g., *Kim et al*., 2011, 2012]. However, recent work has cast shadows on the importance of the humidity-precipitation relationship for MJO simulation [*Klingaman et al*., 2015]. Other factors deemed important for the simulation of the MJO are atmosphere-ocean coupling in the GCM simulations [e.g., *Tseng et al*., 2015] and a more realistic representation of convective heating profiles in the tropics [*Crueger and Stevens*, 2015; *Deng et al*., 2016]. The results of *Klingaman et al*. [2015] question the importance of the latter, though.

Stepping away from MJO-simulation in GCMs, we have learned a great deal about MJO dynamics through the development and application of theoretical models, such as the *multicloud model* used in *Majda et al*. [2007] to produce MJO analogs in a setting resembling non-rotational flows above the equator or the so-called *skeleton model* of the MJO [*Thual et al*., 2014]. Further development of the multicloud model eventually resulted in the SMCM [*Khouider and Majda*, 2008a, 2008b; *Khouider et al*., 2010]—a variant of which we use in this study. Applications of the SMCM so far include investigations of convectively coupled gravity waves in idealized tropical settings [*Frenkel et al*., 2012, 2013], rotational and midtropospheric moisture effects on organized convection [*Majda et al*., 2015], cloud radiative effects, and atmosphere ocean-coupling [*Frenkel et al*., 2015], and the MJO in an aquaplanet general circulation model [*Deng et al*., 2015, 2016]. Further, the SMCM reproduces observed convective behavior in the tropics when using a combination of dynamic and thermodynamic large-scale quantities at 500 hPa to predict tropical convection [*Peters et al*., 2013]. This lead to *Brenowitz et al*. [2015] extending the SMCM to include prognostic nonlocal convergence coupling to predict the occurrence of deep convection—a modification which improves the simulation of equatorial waves.

Based on *Peters et al*. [2013], we couple a modified version of the SMCM into the convection scheme of the comprehensive GCM ECHAM6.3. The implementation is performed in such a way that the convective trigger (the decision of whether shallow, deep, or midlevel convection is simulated) and the closure of the convection scheme is modified. In a nutshell, the SMCM predicts deep convective area fractions $\sigma_d$ at the subgrid scale given vertical pressure velocity and relative humidity at 500 hPa, $\omega_{500}$ and $\mathrm{RH}_{500}$, respectively. Deep convection is triggered for $\sigma_d > 0$ and $\sigma_d$ is then used to calculate the deep convective cloud base mass-flux closure. All other parts of the convection scheme are left untouched. This implementation results in a version of ECHAM6.3 which improves the representation of tropical convection compared to the standard model whilst not degrading the simulated global mean climate too much, i.e., the differences between the two model versions are small compared to the differences with respect to observations/reanalysis data.

The paper is organized as follows: in section 2 we present the implementation strategy for the modified version of the SMCM into the operational convection scheme of ECHAM6.3 and introduce the simulation setups. In section 3, we briefly analyze the global and tropical climate as simulated by the standard and modified setup of ECHAM6.3, with a particular focus on objective methods to quantify simulated TISV and the MJO in particular. We contrast the differences in convective behavior between the two model versions in detail in section 4 to investigate the processes related to the improved representation of tropical convection in the modified version of ECHAM6.3. We discuss a suite of sensitivity experiments and interpret the results in section 5. We conclude with section 6.

## 2. Incorporating the SMCM into ECHAM6.3

In this section, we describe our approach of implementing the SMCM as part of the operational convection scheme of the state-of-the-art GCM ECHAM6.3—a derivative of ECHAM6 which corresponds to the model

version which took part in CMIP5 [*Stevens et al.*, 2013]. Our approach builds upon the results of *Peters et al.* [2013], who tuned and evaluated the SMCM against observations of tropical convection over Darwin and Kwajalein. In doing so, they found that the tuned SMCM is able to reproduce the overall behavior of tropical convection, but overestimates (underestimates) convection for weak (strong) large-scale forcing. In the following, we present a modified version of the SMCM which improves upon the aforementioned issue. Then, we illustrate the implementation of the SMCM into the operational ECHAM6.3 convection scheme. We do not provide an in-depth description of the SMCM, which is available in a number of other publications [e.g., *Khouider et al.*, 2010; *Frenkel et al.*, 2012, 2013; *Brenowitz et al.*, 2015; *Deng et al.*, 2015, 2016].

### 2.1. Modified SMCM Response to External Forcing

The SMCM predicts, constrained by the large-scale atmospheric state, the evolution of a cloud population on a lattice consisting of $n \times n$ square sites by means of a coarse-grained birth-death process evolved in time by means of a computationally optimized acceptance-rejection Markov chain Monte Carlo method [*Khouider et al.*, 2010]. The cloud population consists of three cloud types which are typically associated with tropical convection: congestus, deep convective, and stratiform clouds. At any given point in time, the cloud population is characterized by area fractions per cloud type, which serve as prognostic variables. These cloud types evolve, transition from one to the other, and dissolve according to a set of transition rules and timescales [cf., *Khouider et al.*, 2010]. Tuning of the time scales can be performed either ad hoc as in *Peters et al.* [2013] or quantitatively using e.g., Bayesian methods [*De La Chevrotière et al.*, 2014, 2016]. The atmospheric large-scale state enters the SMCM via two variables, one of which promotes deep convection, denoted C, whereas the other one inhibits deep convection, denoted D. The effect of the atmospheric large-scale state on the transition rates $R_{ab}$ from e.g., cloud type $a$ to cloud type $b$ is described as

$$\Gamma_1(x) = 1 - e^{-x}, \quad x \in [0; 2] \tag{1}$$

with $x$ being either $C$ or $D$ [*Khouider et al.*, 2010]. The transition rates $R_{ab}$ depend on equation (1) as, e.g., $R_{ab} \propto \Gamma(\mathrm{C})\Gamma(\mathrm{D})$. *Peters et al.* [2013] associated $C$ with a measure related to large-scale convergence as

$$C_\omega = -\omega_n \ \omega_{500}, \quad \omega_{500} < 0, \tag{2}$$

where $\omega_{500}$ is the large-scale vertical pressure velocity at 500 hPa and $\omega_n$ a normalization factor to achieve $C_\omega \in [0 : 2]$. Here, $\omega_n = 1.5\,\mathrm{Pa\,s^{-1}}$. We derived this value from a single-column simulation of the TWP-ICE test case (introduced in *Davies et al.* [2013a]) with ECHAM6.2 in which the maximum of $\omega_{500}$ was simulated as $\omega_{500} = -1.4\,\mathrm{Pa\,s^{-1}}$. This scaling may lead to values of $C_\omega > 2$. In such a case, we limit the value of $\Gamma(x)$ to 1. In cases where $\omega_{500} > 0$, we set $C_\omega = 0$. Associating $D$ with midlevel relative humidity as

$$D_{\mathrm{RH}} = 2 \times (1 - \mathrm{RH}_{500}), \quad \mathrm{RH}_{500} \in [0; 1], \tag{3}$$

where $\mathrm{RH}_{500}$ is the relative humidity at 500 hPa, resulted in a promising representation of tropical convection by the SMCM after it had been tuned to achieve a best fit to observed mean convective activity [*Peters et al.*, 2013]. However, the SMCM overestimates (underestimates) tropical deep convective activity for weak (strong) large-scale forcing despite the tuning. *Peters et al.* [2013] pointed out that the functional relationship assumed in equation (1) (Figure 1) is probably responsible for this misrepresentation of convective behavior. We propose that the SMCM's capacity to reproduce observed convective behavior would improve substantially if $\Gamma_1(x)$ were modified as follows:

1. reduce the function's value and gradient for small $x$, i.e., weak large-scale forcing
2. increase the function's value and gradient for large $x$, i.e., strong large-scale forcing.

The above criteria are met by the alternative formulation

$$\Gamma_2(x) = 0.52\ (0.964 + \tanh\ (2(x-1))), \quad x \in [0; 2] \tag{4}$$

illustrated by the dashed line in Figure 1. This alternative formulation is inspired by the approach presented in *Stechmann and Neelin* [2011], who used a *tanh*-relationship to capture the observed increase in convective activity with increasing column water vapor. The exact form of $\Gamma_2(x)$ was determined in an iterative process to most closely satisfy $\Gamma_2(x) \in [0; 1]$.

$\Gamma_2$ significantly reduces the response function's value for $x \in [0; \approx 0.7]$ compared to $\Gamma_1$, features a very steep increase for $x \in \approx [0.7; 1.5]$ and then levels off to attain the maximum value of 1 for $x \approx 2$. Further,

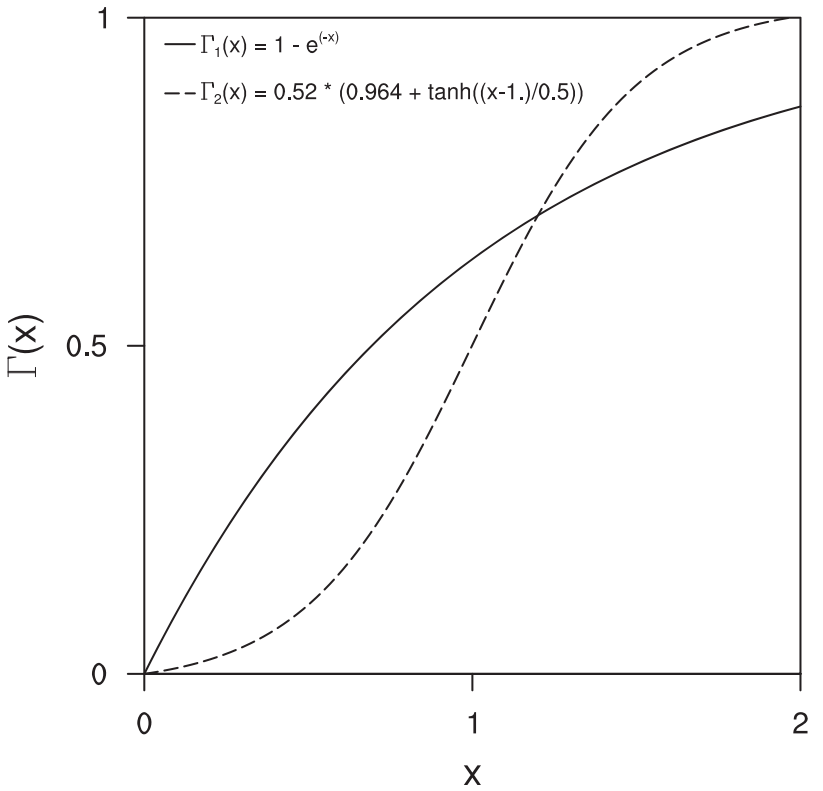


**Figure 1.** Different representations of the internal response function $\Gamma(x)$ used in the SMCM to link the large-scale forcing to the cloud transition rates. The solid line, $\Gamma_1(x)$, corresponds to the standard representation [*Khouider et al.*, 2010]. The dashed line, $\Gamma_2(x)$, is developed in this study. See main text for details.

the value of $\Gamma_1(x)$ remains clearly $< 1$ for the defined range of $x \in [0; 2]$, while $\Gamma_2(x)$ does not. Physically, this implies that using $\Gamma_2(x)$ allows convection to be more strongly forced (or suppressed) in situations of large $C_\omega$ ($D_{\mathrm{RH}}$) and thus more effectively spans the range of forcing used to drive the SMCM compared to $\Gamma_1(x)$. We have performed tests confirming that (i) the SMCM run with $\Gamma_2$ behaves significantly different from a version run with $\Gamma_1$, and (ii) the SMCM run with $\Gamma_2$ more adequately simulates observed convective behavior as presented in *Peters et al.* [2013] (supporting information Text S1 and Table S1).

In the interest of brevity, we now only focus on the SMCM version which employs $\Gamma_2$ for the remainder of this paper.

### 2.2. Implementation into ECHAM6.3 Convection Scheme

#### 2.2.1. The General Idea

We aim to use the SMCM as a tool to predict the deep convective cloud base mass-flux, $M_{cb}$, in a mass-flux convection scheme. Essentially, $M_{cb}$ provides the closure for the convection scheme [e.g., *Tiedtke*, 1989; *Gregory et al.*, 2000].

We propose here to use the SMCM to calculate $M_{cb}$, given by

$$M_{cb} = \sigma_d w_{cb} \rho_{cb}, \tag{5}$$

with $\sigma_d$ the deep convective area fraction, $w_{cb}$ the vertical upward velocity at cloud base and $\rho_{cb}$ the density of air at cloud base. The SMCM can be used to predict $\sigma_d$ given the large-scale state ($C_\omega$, $D_{\mathrm{RH}}$, equations (2) and (3)) and $\rho_{cb}$ is given by the large-scale state of the model. For reasons of simplicity, we assume $\omega_{cb} = 1\,\mathrm{m\ s^{-1}}$ —a value supported by observations [*Kumar et al.*, 2015, 2016]. This simplifying assumption is partially justified by the findings of *Davies et al.* [2013b] that to first-order area (or grid-box) average convective precipitation is driven by the size of the area that is convecting. In future implementations, we intend to calculate an estimate for $w_{cb}$ using a simple model, such as proposed by *Jakob and Siebesma* [2003].

We do not use the SMCM predicted congestus and stratiform area fractions. This is because (i) the congestus area fractions are not well constrained by observations [*Peters et al*., 2013] and (ii) incorporating the often very large stratiform area fractions (often $>0.5$) would involve substantial modifications of the host model's large-scale cloud scheme. Using $\sigma_d$ to describe $M_{cb}$ is an essential step toward overcoming the commonly assumed *scale separation* of convective and large-scale processes in GCMs which breaks down with increasing model resolution [e.g., *Arakawa and Wu*, 2013; *Wu and Arakawa*, 2014]. Although our implementation of the SMCM does not contain a scale-dependent formulation for $\sigma_d$, it is a step toward the design of a novel-scale aware convection parameterization. Ongoing work by two of the authors (B.M. and C.J.) focuses on extending the work presented here towards a true scale aware convection parameterization built around the SMCM concept.

A very similar approach as the above was recently taken by *Dorrestijn et al*. [2016]. They coupled data-driven Markov chain-based stochastic models of convective area fractions (formally derived in *Dorrestijn et al*. [2015] and *Gottwald et al*. [2016]) to the convection scheme of a GCM of intermediate complexity. They found that the simulations using the modified convection schemes displayed improved representations of TISV when compared to the standard model version. Here we investigate if this conclusion still holds in a full complexity GCM.

Our approach presented here differs substantially from previous implementations of the SMCM into GCMs. *Deng et al*. [2015] and *Deng et al*. [2016] coupled the SMCM to a simple GCM in an aquaplanet setting in which all physical processes apart from upper tropospheric and boundary layer damping were turned off (based on *Khouider et al*. [2011]), with the SMCM providing parameterized heating rates derived from the convective cloud population (congestus, deep, stratiform). *Goswami et al*. [2016] implemented the SMCM into the fully coupled Climate Forecast System version 2 (CFSv2) through the use of prescribed vertical profiles of heating and drying obtained from observations.

#### 2.2.2. The SMCM in the ECHAM6.3 Convection Scheme

ECHAM6.3 can be run with the "original" convection parameterization following *Tiedtke* [1989] or with a variant thereof proposed by *Nordeng* [1994], which is the current standard setting and which we refer to as the "convection scheme" in the following [see *Möbis and Stevens*, 2012 for an overview]. The convection scheme computes either shallow, deep, or midlevel convection given the large-scale environment. Convection is diagnosed to occur if (i) an air parcel (whose temperature depends on the standard deviation of temperature in the lowest model level) lifted from the lowest model level to its lifting condensation level (LCL) is buoyant at every level, (ii) the vertical integral of water vapor tendency from the surface to the LCL is positive, and (iii) the total water in the lifted parcel exceeds that of the environment at the LCL by a certain threshold [*Möbis and Stevens*, 2012]. If the column integrated moisture convergence exceeds the surface latent heat flux by more than 10%, deep convection is assumed to occur—shallow convection is calculated otherwise ("deep-shallow-trigger"). This criterion is rooted in the assertion by *Tiedtke* [1989] that in shallow convective regimes, the moisture supply to cumulus clouds is regulated by surface evaporation and that large-scale moisture convergence is negligible. Among others, deep and shallow convection modes differ in their respective assumed entrainment profiles, i.e., entrainment rates $\varepsilon$ are larger for shallow ($\varepsilon_{sc}=3\times10^{-3}$ m$^{-1}$) compared to deep convection ($\varepsilon_{d}=1\times10^{-4}$ m$^{-1}$). The convective updraft calculation is performed twice using the result of the deep-shallow-trigger for the first iteration. If a deep convective updraft is calculated in the first iteration but the distance between LCL and the level of neutral buoyancy is 200 hPa or less, shallow convection is assumed for the second iteration. Midlevel convection is performed if neither deep nor shallow convection can be triggered.

For deep convection, the calculation of the closure of the convection scheme ($M_{cb}$) is based on an equilibrium assumption such that it relaxes the vertically integrated buoyancy of the updraft, essentially a measure of CAPE, to zero within a prescribed decay time currently set to 2 h. A detailed description of the closure formulation is provided in *Möbis and Stevens* [2012].

Our implementation of the SMCM into the convection scheme modifies the deep-shallow-trigger as well as the closure formulation. A schematic of our implementation of the SMCM into ECHAM6.3 is shown in Figure 2. The SMCM is set up following *Peters et al*. [2013], with the cloud-type transition timescales equal to those reported for case "$C_\omega$" in their Table 1. $n$ is set to 20, yielding $n\times n=400$ lattice sites which corresponds to a lattice edge length of approximately 10 km at the host model resolution used here. We performed sensitivity tests to investigate the impact of the number of lattice sites: fewer lattice sites ($n=10$) increase the

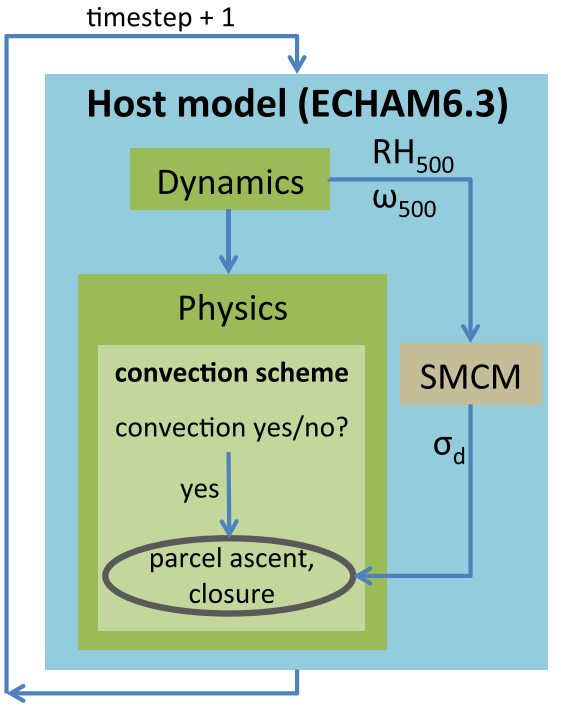


**Figure 2.** Schematic illustrating the implementation of the SMCM as part of the ECHAM6.3 convection scheme on the scale of a model grid box. "Dynamics" refers to the calculations by the dynamical core, which are performed in spectral space, whereas "Physics" refers to the whole suite of physical parameterizations, one of which is the convection scheme. $\omega_{500}$ and $RH_{500}$ refer to vertical pressure velocity and relative humidity at approximately 500 hPa as provided by the model dynamics, respectively. The SMCM itself is run with an internal time step shorter than that of the host model and has knowledge of the convective state from the previous host model time step. See main text for details.

variability of SMCM-simulated $\sigma_d$, resulting in a wider spread of simulated $\sigma_d$; more lattice sites ($n = 40$) reduce the variability and spread of simulated $\sigma_d$. This is the expected behavior as variability increases for small $n$ and the SMCM reaches its deterministic limit for large $n$ (Q. Deng, personal communication, 2016). We discuss the impacts of changing $n$ in section 5 and the supporting information.

We apply the SMCM globally and it evolves a different convective cloud population in every host model grid box. As the SMCM employs a Markov-process approach to simulate the occurrence of atmospheric convection, making it part of the convection scheme incorporates convective memory at the grid scale—an important feature missing in most current convection schemes which might have important implications for adequately representing convective organization [e.g., *Tan et al.*, 2015]. The SMCM is invoked once every GCM time step (7.5 min), which is a value similar to the one we used in *Peters et al.* [2013] (5 min). The SMCM then performs internal time stepping, where the exact number of internal iterations performed by the SMCM depends on the large-scale forcing and the current transition probabilities between the cloud types and is determined as described in *Gillespie* [1975].

Whenever convection is diagnosed to occur and $\sigma_d > 0$, we let the convection scheme perform calculations as if deep convection were diagnosed by the deep-shallow-trigger. If the convection scheme is invoked but $\sigma_d = 0$, we enforce shallow convection and there is no chance to revert to deep convection. We have applied no changes to the part of the convection scheme which treats shallow convection.

$\sigma_d$ is then used to prescribe $M_{cb}$ according to equation (5), assuming a fixed value of $\omega_{cb} = 1\ \mathrm{m\ s^{-1}}$ (as also done in *Dorrestijn et al.* [2016]). The choice of $\omega_{cb} = 1\ \mathrm{m\ s^{-1}}$ is well supported by observations of tropical convection [*Kumar et al.*, 2015, 2016].

### 2.3. Experiment Setup and Data

We utilize ECHAM6.3 at T63 horizontal resolution ($\approx 1.8° \times 1.8°$) with 47 vertical levels extending from the surface to 0.01 hPa, which corresponds to a height of roughly 80km. The standard physical parameterization schemes as described in *Stevens et al.* [2013] are used.

We perform and analyze 30 year AMIP-style climate simulations using either the standard convection scheme [*Tiedtke*, 1989; *Nordeng*, 1994], E63-REF, or the above described version coupled to the SMCM, E63-SMCM. The simulations cover the time period of 1978–2008 (1978 is considered as model spin-up and disregarded for analysis). Global sea surface temperatures and sea ice concentrations (monthly) are prescribed according to AMIP II specifications [*Taylor et al.*, 2000], greenhouse gas concentrations follow observed and RCP4.5 concentrations for the pre and post-2000 period, respectively. Natural and anthropogenic aerosols are prescribed following *Kinne et al.* [2013]. Atmospheric coupling to the land surface is calculated using the submodel JSBACH [*Reick et al.*, 2013]. The model time step is 7.5 min and we store 6 h averages of model output.

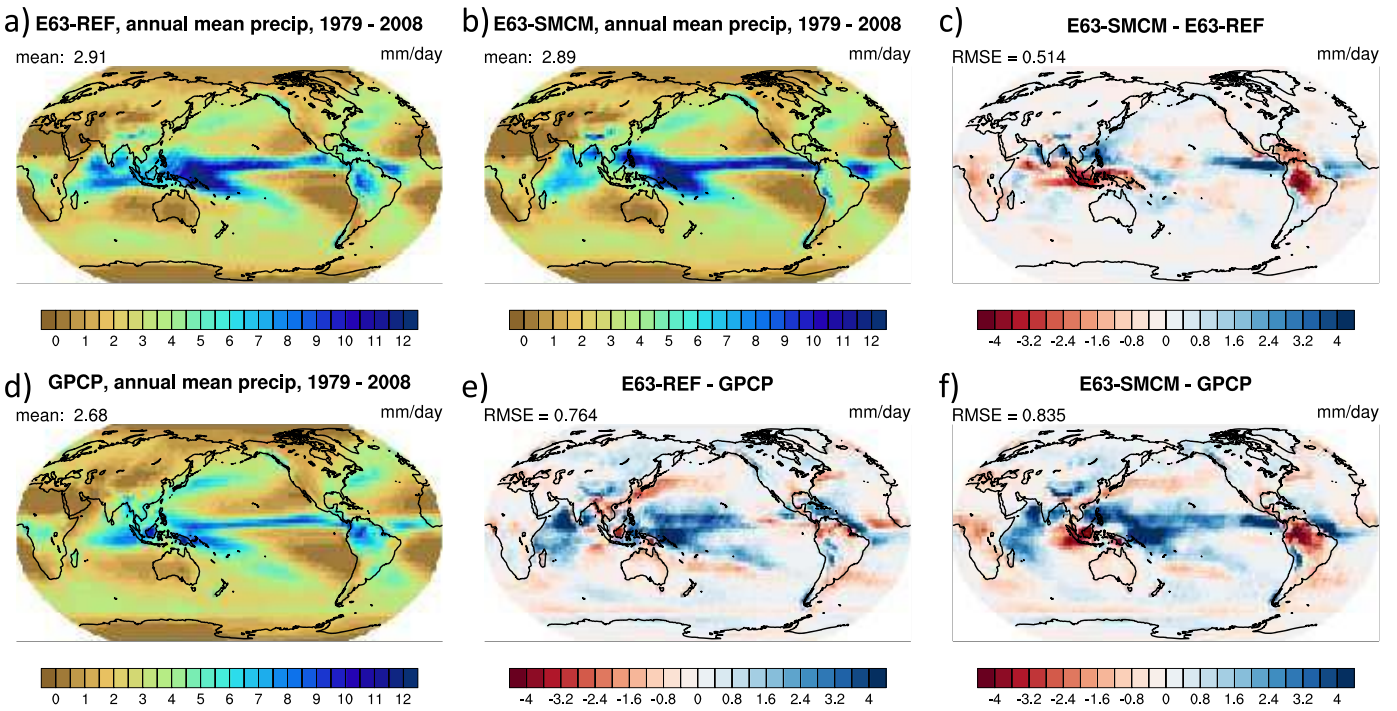


**Figure 3.** Annual mean total precipitation for experiments E63-REF and E63-SMCM and comparison to observations (GPCP) for the period of 1979–2008. (a) E63-REF, (b) E63-SMCM, (c) difference between the experiments (E63-SMCM and E63-REF), (d) GPCP and differences of the experiments compared to GPCP (e) and (f). GPCP data are from the v2.2 monthly product [*Adler et al.*, 2003].

For detailed analyses of simulated convection in both model setups, we also perform simulations with both versions storing output for each time step. For those experiments, the year 2002 is simulated for model spin-up and we store time step data for January 2003.

For evaluation of model performance, we use ERA-Interim reanalysis data [*Dee et al.*, 2011] for atmospheric parameters and estimates of surface rainfall as provided by GPCP (versions 1.2 and 2.2 for daily and monthly data, respectively) [*Huffman et al.*, 2001; *Adler et al.*, 2003]. Outgoing longwave radiation (OLR) data is obtained from Advanced Very High Resolution Radiometer (AVHRR) measurements [*Liebmann and Smith*, 1996].

## 3. Global and Tropical Climate

We begin our evaluation by first assessing the performance of both model versions in terms of the mean simulated climate. Then, we specifically investigate the model performance in terms of simulated tropical climate and provide evidence of a substantially improved simulation of MJO-like features and CCEWs in experiment E63-SMCM compared to E63-REF.

### 3.1. Global Mean Climate

Annual mean precipitation patterns are very similar among both model versions (Figures 3a and 3b), with E63-SMCM producing slightly less rainfall than E63-REF related to changes in the global mean energy budget of the atmosphere (see below). E63-SMCM shows a pronounced drying of the Maritime Continent region as well as over tropical and subtropical land areas such as Africa and South America (Figure 3c). Changes in midlatitude precipitation are negligible. Overall, E63-SMCM inherits much of the biases already present in the standard model setup (Figures 3e and 3f) [*Stevens et al.*, 2013 their Figure 7], with exacerbated errors over the Maritime Continent and the Amazon, though.

Time step data reveal that especially over tropical South America, E63-SMCM shows substantially less deep convective and more shallow events compared to E63-REF (not shown). This is because the SMCM rarely predicts $\sigma_d > 0$ in this region, thus inhibiting the calculation of deep convection. Over land, surface properties impose strong controls on precipitation [e.g., *Pielke*, 2001; *Koster et al.*, 2004]. As the SMCM predicted $\sigma_d$

solely depends on the large-scale environment at 500 hPa, hence far away from the surface, its performance over land deteriorates compared to over the oceans where near-surface effects play a smaller role compared to the large-scale. This will be an area for further improvement of the SMCM.

E63-SMCM shows an overall moistening of the lower and drying of the middle and upper tropical troposphere, an increase in cloud liquid water in the tropical lower troposphere (mainly between 600 and 800 hPa), and overall downward shift of cloud ice contents (not shown). Cloud fraction increases (<5%) in the tropical lower and middle troposphere, but decreases at high altitudes (not shown). All these changes are related to the overall reduced strength of deep convection in E63-SMCM (cf., section 4), which is also manifested in a cooler tropical troposphere (not shown). E63-SMCM displays a greater energy imbalance at the top-of-atmosphere (TOA) than E63-REF as no retuning of this balance is performed. The energy imbalance is still inside of what can be considered a useful model (E. Roeckner, personal communication, 2015). Coming back to precipitation, there are some noteworthy differences in simulated precipitation on shorter, i.e., daily timescales. We show probability densities of simulated and observed daily mean precipitation values in the tropics in Figure 4. Compared to GPCP, E63-SMCM overestimates the occurrence of stronger precipitation intensities; E63-REF compares better to GPCP (Figure 4a). Figure 4b shows the fraction of total precipitation per rain rate contributed by each bin [cf., *Holloway et al*., 2012 their Figure 2]. This allows to evaluate whether the simulated precipitation data follow observed rain rate distributions with a power-law relationship of −1 for low values of precipitation [*Peters et al*., 2010], as indicated by the dashed line in Figure 4a. For such a power-law relationship, there should be an equal contribution of precipitation from all weak precipitating events [*Holloway et al*., 2012]. This is mostly true for GPCP and E63-SMCM precipitation, whereas E63-REF shows a pronounced maximum around 10 mm $d^{-1}$. *Holloway et al*. [2012] dubbed such features a "preferred rainfall rate" and found very similar results for model runs with parameterized convection, but not in simulations with explicit convection.

A major difference in simulated precipitation between the two model versions is the fraction of total precipitation attributable to convective or large-scale processes. In E63-SMCM, deep convection is weaker compared to E63-REF (cf., section 4), resulting in a larger contribution to total precipitation from the large-scale cloud scheme. This is especially true in the tropics (not shown). Probability densities of simulated large-scale rainfall (Figure 4c) show higher occurrences for all but the smallest values compared to E63-REF, indicating that stratiform processes play a larger role in E63-SMCM. The results of *Peters et al*. [2013] and the review presented in *Houze* [1997] indeed support a large contribution of stratiform rainfall in the tropics.

### 3.2. Convectively Coupled Equatorial Waves and the Madden-Julian Oscillation

As the design of the SMCM is inspired by the morphology of organized tropical convection [*Khouider et al*., 2010], the representation of CCEWs and the MJO in a GCM may be altered and possibly even improved,

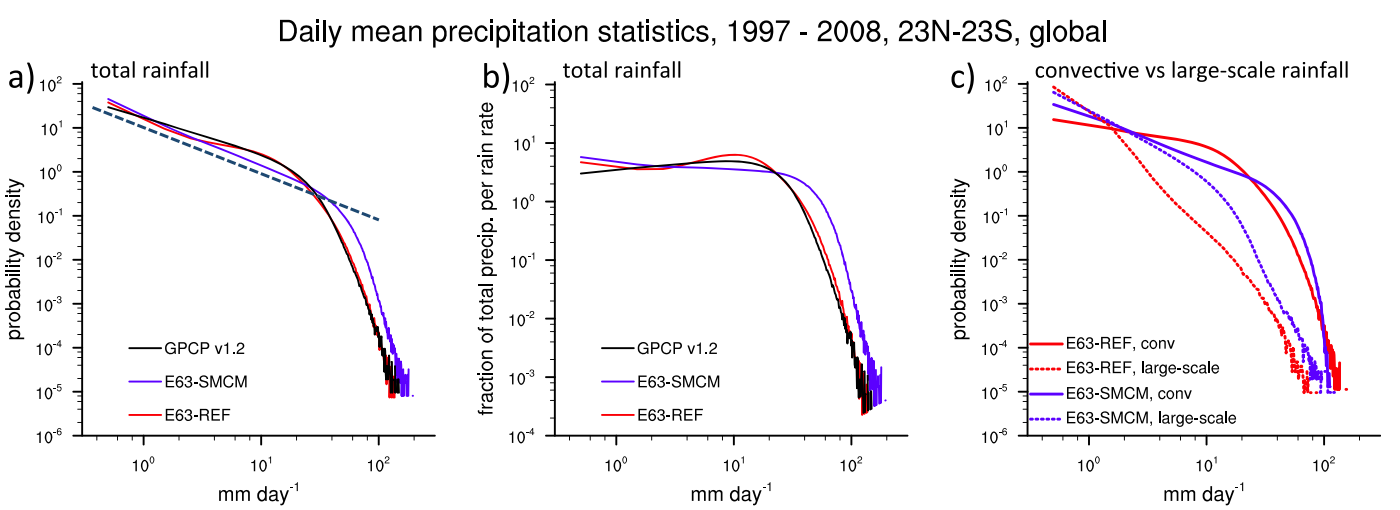


**Figure 4.** Statistics of daily mean precipitation in the tropics (23°N-23°S) from the two model simulations and observations (GPCP). (a) Probability densities of daily mean total precipitation, the dashed line indicates a power-law fit with exponent −1 (see text for details); (b) fractional rainfall amount densities [cf. *Holloway et al*., 2012] for GPCP (black), E63-REF (red), and E63-SMCM (blue); (c) probability densities of daily mean convective (solid) and large-scale rainfall (dashed) for E63-REF (red) and E63-SMCM (blue). GPCP data are from the vn1.2 daily product [*Huffman et al*., 2001] and were remapped to the resolution of the model data prior to analysis. The time period analyzed is 1997–2008.

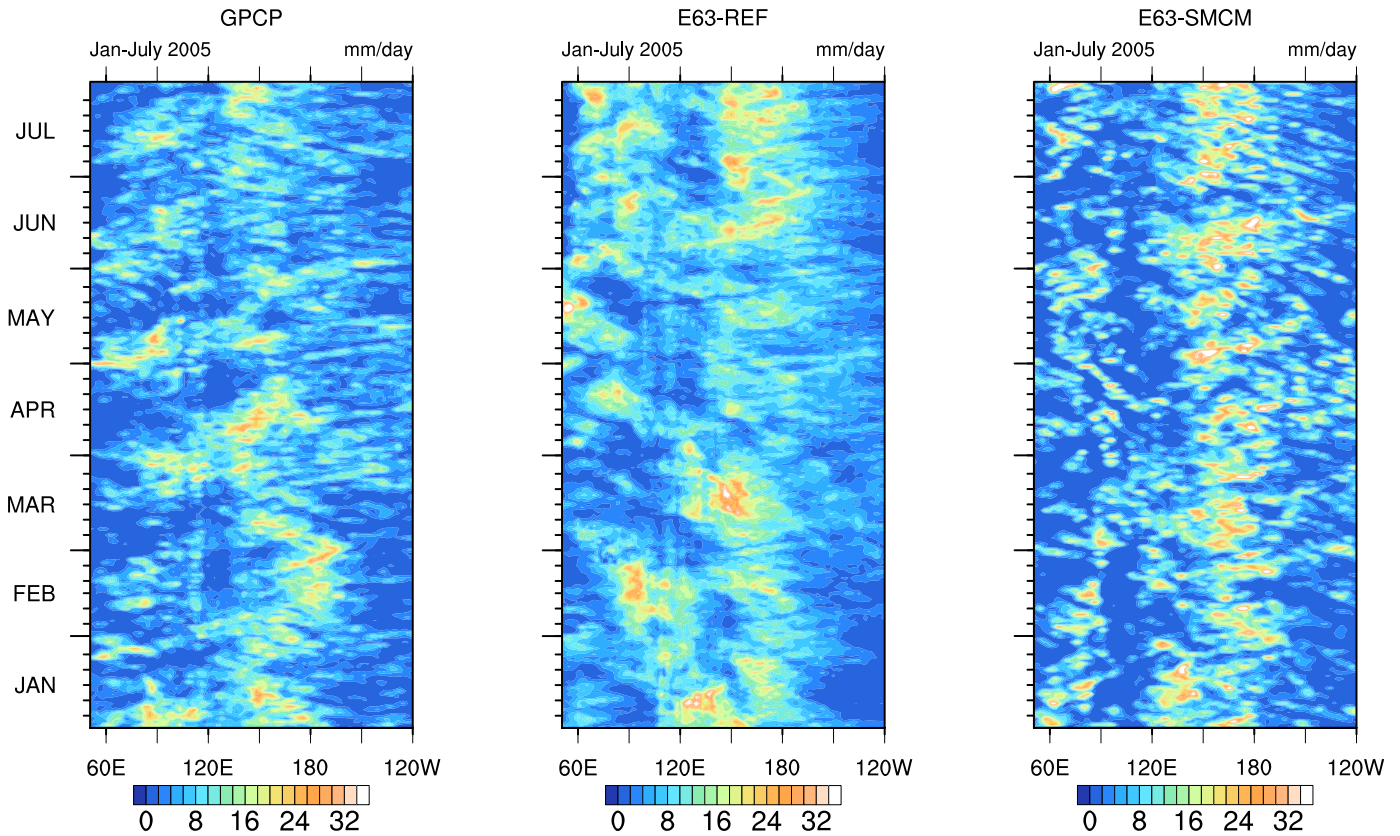


**Figure 5.** Hovmöller diagrams of daily mean total surface rainfall for the period January–July 2005 in the tropics (10°N-10°S, 50°E-120°W): (a) GPCP, (b) E63-REF, and (c) E63-SMCM.

especially when coupling it to model dynamics rather than thermodynamics [cf., *Brenowitz et al*., 2015 for a theoretical perspective]. We thus focus our analysis of experiments E63-REF and E63-SMCM on the representation of organized tropical convection and compare the results to a combination of observations and reanalysis data.

The introduction of the SMCM into ECHAM6.3's operational convection scheme (cf., section 2.2) improves the spatiotemporal coherence of tropical precipitation as we will demonstrate utilizing Hovmöller diagrams of daily mean total surface rainfall and lag-autocorrelations of daily mean rainfall. The simulation of CCEWs and features with spatial and temporal scales corresponding to those of the MJO is also improved as we will demonstrate by use of wavenumber-frequency spectra of outgoing longwave radiation (OLR) at the top of the atmosphere [*Wheeler and Kiladis*, 1999] and a multivariate EOF-analysis [*Waliser et al*., 2009].

We show Hovmöller diagrams of daily mean total surface rainfall for the period of January–July 2005 from observations (GPCP) and the two model experiments in Figure 5. The observations (Figure 5a) illustrate the typical picture of east and westward propagating CCEW's and a pronounced MJO envelope slowly propagating eastward during March–April, starting around 90°E and dissipating close to 180°E. Observed precipitation is often organized in distinct propagating clusters, with nonprecipitating periods between them. In E63-REF (Figure 5b), surface rainfall appears smeared-out compared to GPCP. In E63-SMCM (Figure 5c), surface rainfall appears much more organized and intermittent on smaller scales than in E63-REF. Propagating precipitation clusters—as those seen in observations—are evident. MJO-like behavior is not readily identifiable from the Hovmöller diagrams for both simulations. A quantitative assessment of the simulation of TISV and MJO-like features in particular is presented later in this section.

Lag-autocorrelations $\alpha_{p,d}(\tau)$ of total rainfall in the tropics on daily timescales at the model grid point scale are displayed in Figure 6a. E63-REF displays too high $\alpha_p(\tau)$ at lags $\tau > 2$ days, whereas $\alpha_p(\tau)$ for E63-SMCM is hardly discernible from that of the observations (GPCP). This confirms the impression gained from Figure 5, namely that tropical rainfall is not intermittent enough in E63-REF on daily timescales. The propagation of

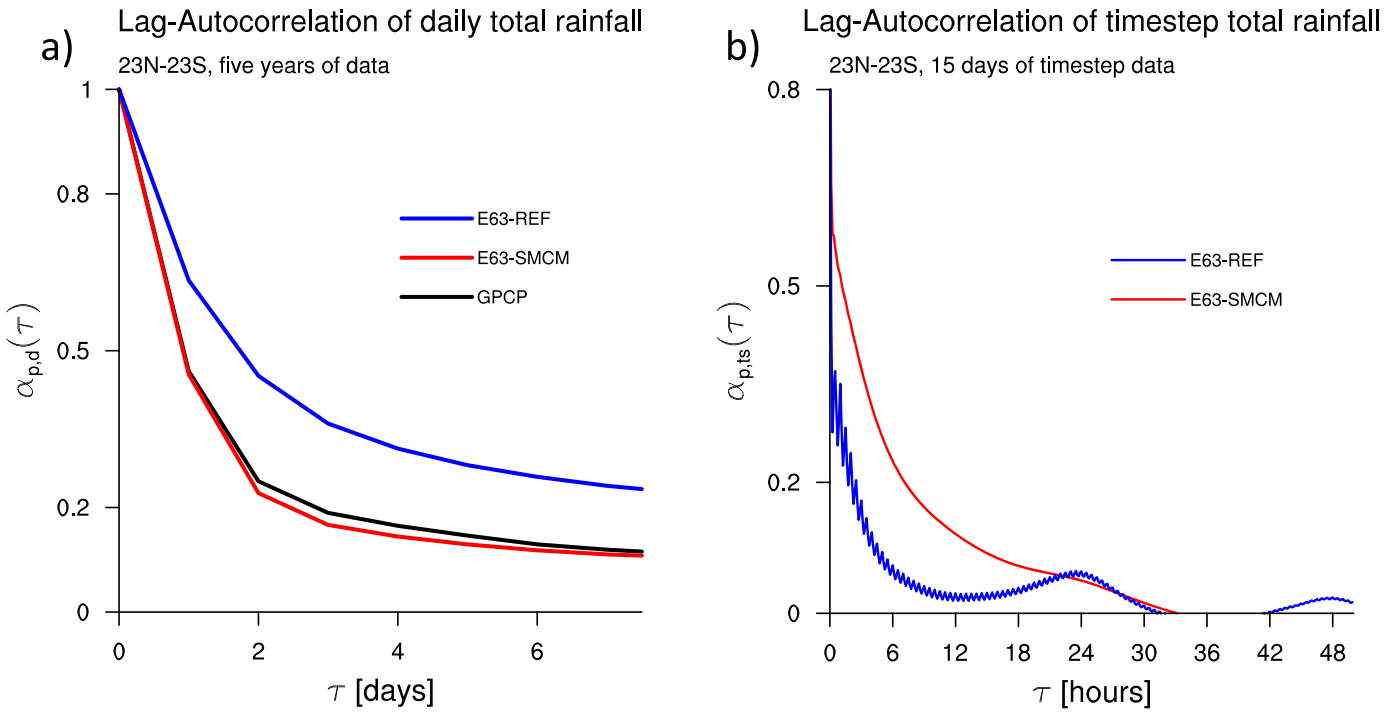


**Figure 6.** Mean lag-autocorrelation $\alpha_p(\tau)$ of total precipitation in the tropics (23°N–23°S) at the model grid box scale in experiments E63-SMCM (red) and E63-REF (blue) compared to observations (GPCP, black). (a) Daily mean total precipitation, 5 years of data are used (1979–1983 for models, 2002–2006 for GPCP); (b) time step total precipitation, 15 days of data. The GPCP data were remapped to the model grid (T63) prior to analysis.

spatially coherent precipitation clusters in observations and E63-SMCM accounts for the low values of $\alpha_p(\tau)$ at lags $\tau > 2$ days (cf., Figure 5).

Figure 6b shows the lag autocorrelation of time step rainfall $\alpha_{p,ts}(\tau)$ for the same tropical domain as in Figure 6a. For E63-REF, $\alpha_{p,ts}(\tau)$ is generally lower than for E63-SMCM, with the exception of local maxima at multiples of $\tau = 24$ h. Also, tropical rainfall in E63-REF shows substantial time step to time step variability which is reflected in a sawtooth pattern of $\alpha_{p,ts}(\tau)$. Using a new introduced diagnostic framework, *Klingaman et al.* [2017] show that such large time step to time step variability of surface rainfall is a common feature in many GCMs. Here, the variability is carried by the convective part of the total rainfall (not shown) and is not present in E63-SMCM which could be due to the incorporation of convective memory at the grid scale. The local maxima of $\alpha_{p,ts}(\tau)$ at multiples of $\tau = 24$ h explain the high autocorrelations of daily mean rainfall for E63-REF shown in Figure 6a. Sensitivity tests show that the larger values of $\alpha_{p,ts}(\tau)$ in E63-SMCM are due to reduced deep convective mass fluxes compared to E63-REF (cf., section 5). The sawtooth pattern in E63-REF however still appears for substantially reduced convective mass fluxes (cf., supporting information Figure S5b).

We continue our investigation of tropical variability by investigating the wavenumber frequency spectra of the symmetric part of the data (daily mean OLR) in Figure 7. In the observations, the most dominant characteristics are the eastward propagating Kelvin waves and the MJO, the latter appearing for periods longer than 30 days and wavenumbers up to 3. The westward propagating equatorial Rossby and inertial gravity waves reveal comparably smaller power. Except for the MJO, all these waves fit the theoretical solutions of the modified shallow water equations [*Matsuno*, 1966; *Kiladis et al.*, 2009].

Both model simulations generally show weaker signals of these phenomena—apart from the equatorial Rossby waves in E63-REF which appear stronger than those in observations. The Kelvin Waves in E63-REF do not fit the theoretical solutions for the given equivalent depths (Figure 7b)—the Kelvin waves in E63-SMCM do however (Figure 7c). This is manifested in an overall slow-down and higher spectral power of Kelvin waves in E63-SMCM compared to E63-REF. Also in contrast to E63-REF, the weak power for small wavenumbers is more realistically simulated in E63-SMCM. The equatorial Rossby waves in E63-SMCM (E63-REF) are weaker (stronger) compared to observations. In addition, the spectral peak in the MJO-range in both

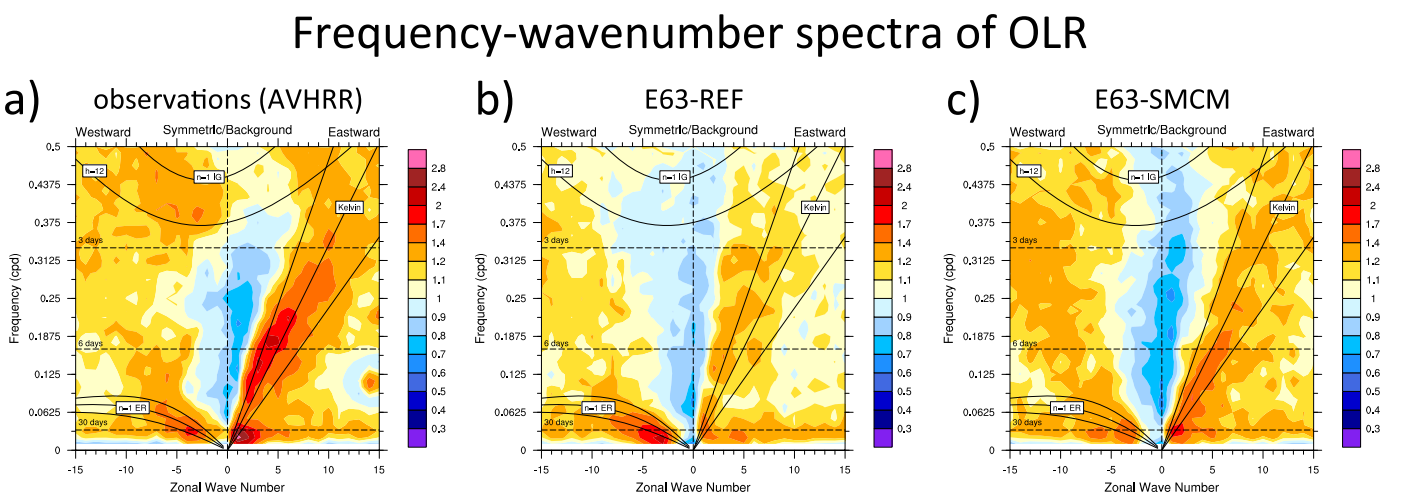


**Figure 7.** Wavenumber-frequency-spectra (symmetric component) of outgoing longwave radiation (OLR) anomalies in the tropics (13°N-13°S). (a) AVHRR, (b) E63-REF, and (c) E63-SMCM. The considered time periods are 1997–2008 (AVHRR) and 1980–1999 (model simulations). The straight lines in the Kelvin wave range indicate, from right to left, theoretical solutions for equivalent depths of 12, 25, and 50 m.

model experiments is generally much weaker than in observations, but stronger in E63-SMCM than in E63-REF.

For a more accurate assessment of the MJO, we calculate multivariate empirical orthogonal functions (EOF) from the outgoing longwave radiation (OLR), and the zonal wind at 850 (u850) and 200 hPa (u200) following *Waliser et al*. [2009] and *Crueger et al*. [2013].

We show the life cycle of the MJO separated into eight phases as constructed by compositing the u850 winds and OLR over the sum of the square of the first two principal components PC1 and PC2 of the multivariate EOFs in Figure 8—a more detailed analysis of PC1 and PC2 is provided in Figure 9 and discussed later. The eight phases of the MJO life cycle are obtained from the phase relationship between PC1 and PC2 [*Wheeler and Hendon*, 2004; *Waliser et al*., 2009]. In reanalysis data, the first two MJO phases (Figures 8a rows 1 and 2) are characterized by enhanced convection over the Indian Ocean with easterly winds and suppressed convection prevailing east of the enhanced convection, i.e., over the warm pool area. During the mature phases of the MJO (Figure 8a, rows 3–6), the convective signal intensifies (phases 3 and 4) and propagates eastward over the Maritime Continent while being accompanied by westerly near-surface winds. At the same time, suppressed convection begins to prevail over the Indian Ocean. Later stages of the MJO (Figure 8a, rows 7-8) show dissipating deep convection near the date line. A strong phase-relationship between OLR and near-surface winds is apparent throughout the evolution of the MJO (Figure 8a).

From Figures 8b and 8c, it is evident that the simulation of MJO-like features is improved in E63-SMCM compared to E63-REF. For E63-REF (Figure 8b), the convective signature is characterized by a sign switch of the anomalies between phases 2–4 and 6–8 with no evident eastward propagation. This is also evident from the low cross correlations between PC1 and PC2 and the fact that the convective signal is dominated by EOF2, which reveals one maximum of enhanced and one maximum of suppressed convection (Figure 9). In addition, the wind signal is very weak, indicating a lack of coupling between convection and circulation. In contrast, E63-SMCM (Figure 8c) reveals a convective disturbance which evolves in the Indian Ocean, propagates eastward and decays near the date line. This is comparable to the structures identified in the reanalysis data (Figure 8a), albeit the convective signal being much weaker in E63-SMCM. The coupling to the circulation is strengthened in E63-SMCM as evidenced by a considerable wind signal resembling that derived from reanalysis data.

To further quantify the MJO in reanalysis data and the capacity of the two model setups to simulate MJO-like features, we show the leading pairs of EOFs of OLR, u850, and u200 as well as the cross-correlation between them in Figure 9. From the reanalysis data (Figure 9 top row), the following main MJO signatures are evident:

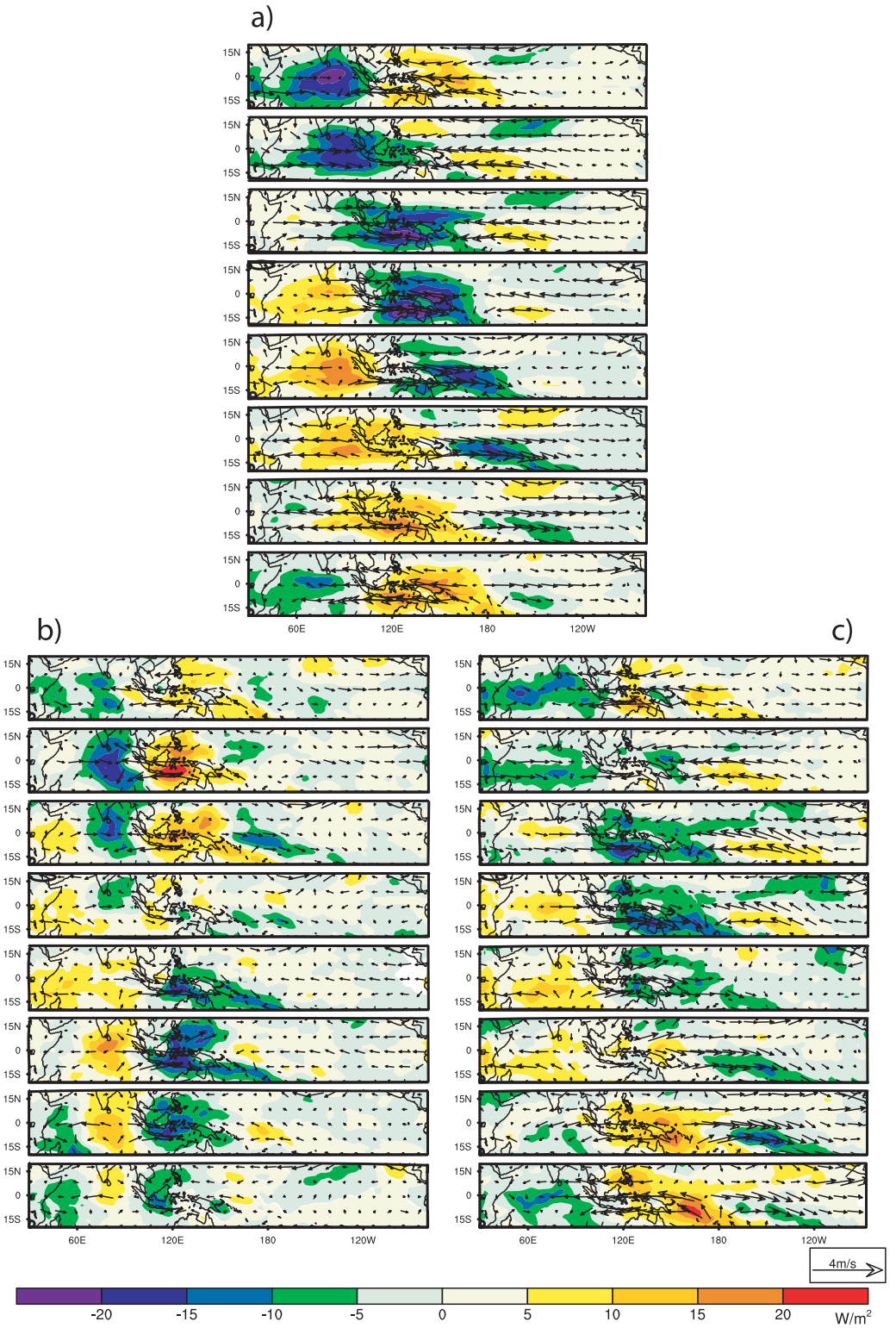


**Figure 8.** Composite November–April 20–100 day-filtered OLR (blue/green: enhanced convection; yellow/orange: suppressed convection) and 850 hPa wind anomalies (vectors) as a function of MJO phase. The composites are based on $PC1^2 + PC2^2 > 1$ (see text for more information) and cover the time period of 1980–1999. (a) ERA-Interim, (b) E63-REF, and (c) E63-SMCM.

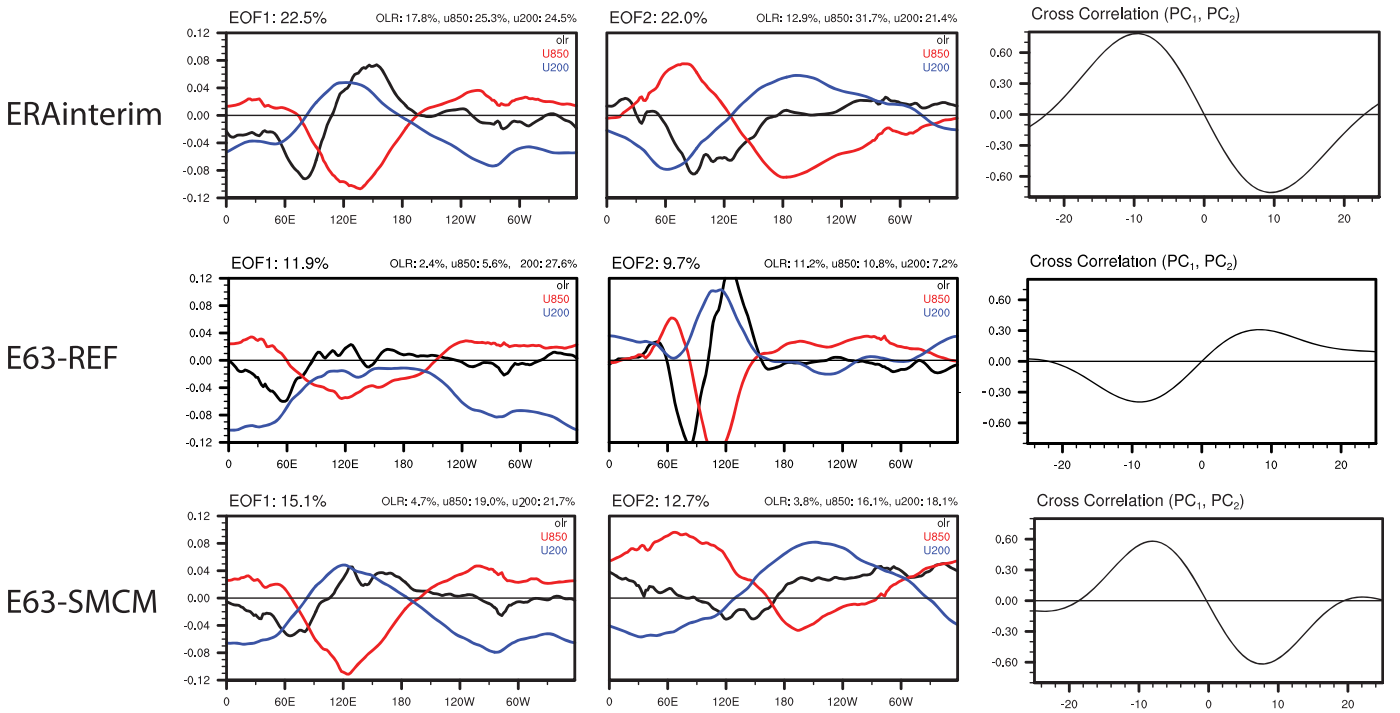


**Figure 9.** Leading pairs of multivariate empirical orthogonal functions (EOF1, EOF2) of outgoing longwave radiation (OLR, black) and zonal winds at 850 (u850, red) and 200 (u200, blue) hPa and the lead-lag cross-correlations between their principal components (PC1, PC2). Results are shown for (top) ERA-Interim, (middle) E63-REF, and (bottom) E63-SMCM. Portions of explained total variance (average and per variable) by the EOFs are indicated in the panel headers. The analysis follows *Waliser et al*. [2009] and is restricted to the inner tropics (15°S–15°N). The time period considered is 1980–1999.

1. a zonal overturning circulation indicated by the out-of-phase relationship between the u850 and u200 anomalies, having always different signs;
2. positive (westerly) u850 anomalies west of enhanced convection over the Indian Ocean;
3. zonal wind anomalies more in phase with enhanced convection in the west Pacific;
4. strong OLR anomalies only in the eastern hemisphere, whereas the circulation anomalies are strong around the entire equator;
5. roughly the same portion of intraseasonal variance in the two leading EOFs for the total and the partial variances; and
6. a strong lag-correlation between the principal components at around 10 days (0.8), indicating the eastward propagation of the convectively coupled circulation system.

These features are missing or at least distorted in E63-REF: although there is a rough out-of-phase relationship between u850 and u200, there is no circumferential overturning circulation, because the opposite sign of u850 and u200 is partly missing. A relationship between the position of convection and wind anomalies is also evident, however distorted. This leads to strongly different structures between the patterns and different amounts of explained partial variances. As a consequence, the lag-correlation is small (0.4), i.e., there is hardly any propagation.

Compared to E63-REF, E63-SMCM shows a clear improvement regarding the simulation of MJO-like disturbances. u850 and u200 reveal an out-of-phase relationship and thus represent a zonal overturning circulation. Both EOFs reveal roughly similar patterns and similar amounts of explained variance. The lag-correlation between the principal components is considerably higher (0.63), implying a strong coupling between the two EOFs and a pronounced eastward propagation.

The main failures in both model versions are the too small amounts of explained variance, especially the partial variance for $F_{OLR}$. This is however a common failure of most GCMs [*Waliser et al*., 2009]. A quantitative assessment of the MJO performance can be obtained from an MJO-index ($MJO_{ind}$), introduced by *Crueger et al*. [2013]:

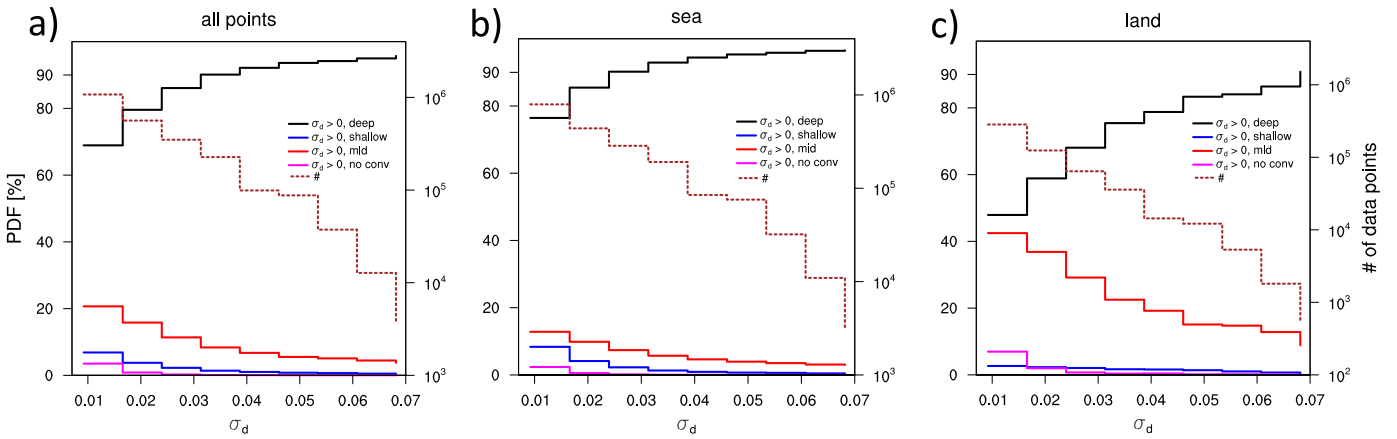


**Figure 10.** PDFs of final convective type per time step for cases of $\sigma_d > 0$ as function of $\sigma_d$. Solid curves represent PDFs (left y Axis), dashed curves represent number of cases (right y Axis). (left) All points, (middle) sea, and (right) land. All available time step data for January 2003 are used; the analysis is restricted to the inner tropics (23°N–23°S).

$$MJO_{ind} = \sqrt{(max(1, R_{mean}) - 1) * \frac{F_{OLR}}{100}} \tag{6}$$

Here, $R_{mean}$ represents a measure for the strength of the eastward propagation of the wave, averaged for OLR, u850, and u200. The eastward propagation of a single variable is measured by the ratio of the power in eastward versus westward moving features within the MJO wavenumber/frequency ranges, which (following *Waliser et al.* [2009]) we choose to be the wavenumbers 1–3 and frequencies $100^{-1}$–$20^{-1}$ $d^{-1}$. Calculating the MJO-index for the reanalysis gives a value of 1.0, whereas the data from E63-REF and E63-SMCM yield values of 0.0 and 0.33, respectively. This quantitatively confirms the qualitative MJO assessment, namely that E63-SMCM shows considerable improvements in the simulation of MJO-like features compared to E63-REF, albeit much weaker than those identified in reanalysis data. In the following, we will thus refer to E63-SMCM being able to simulate the "MJO" instead of just "MJO-like features."

## 4. SMCM-Impacts on ECHAM6.3 Convection: The Details

The previous sections have shown that the implementation of the SMCM in ECHAM6.3 has had large effects on the model's tropical variability, with some additional impacts on the tropical mean climate especially over land. It is difficult to understand the causes for these changes without an in-depth investigation of the behavior of the convection scheme itself. To do so, we present time-step level (7.5 min) and daily averaged data to illustrate the different behavior of the two convection implementations.

As detailed in section 2.1, the SMCM estimates deep convective area fraction $\sigma_d$ at every time step and GCM model grid box. Even when the SMCM simulates $\sigma_d > 0$, the decision to perform deep convection may be overridden in the iterative decision process internal to the convection scheme if the convective cloud is not deep enough [cf., *Möbis and Stevens*, 2012 and section 2.2]. To investigate how often this is the case, we show probability distribution functions (PDFs) of the final convective type for all cases of $\sigma_d > 0$, including "no convection," on a time step basis as function of $\sigma_d$ in Figure 10.

Several points immediately catch the eye in Figure 10. The frequency of simulated values of $\sigma_d$ is approximately log-normally distributed, in agreement with observations in the tropics [e.g., *Gottwald et al.*, 2016]. The success rate for deep convection to actually be calculated for $\sigma_d > 0$ (solid black lines in Figure 10) increases with increasing values of $\sigma_d$. Success rates over ocean are generally higher than over land, with values >90% for $\sigma_d >\approx 0.025$ over ocean. Over land, success rates only reach values of about 90% for very large values of $\sigma_d$. Success rates over land are lower than over ocean because (i), *Peters et al.* [2013] trained the SMCM using observations resembling oceanic/coastal regimes and (ii) because the SMCM at this stage does not consider any information about the state of the surface and the planetary boundary layer. This is clearly a weakness of the current implementation of the SMCM that will require addressing in future work. As a consequence, the SMCM often predicts nonzero $\sigma_d$ over arid regions, such as the Sahara desert (not

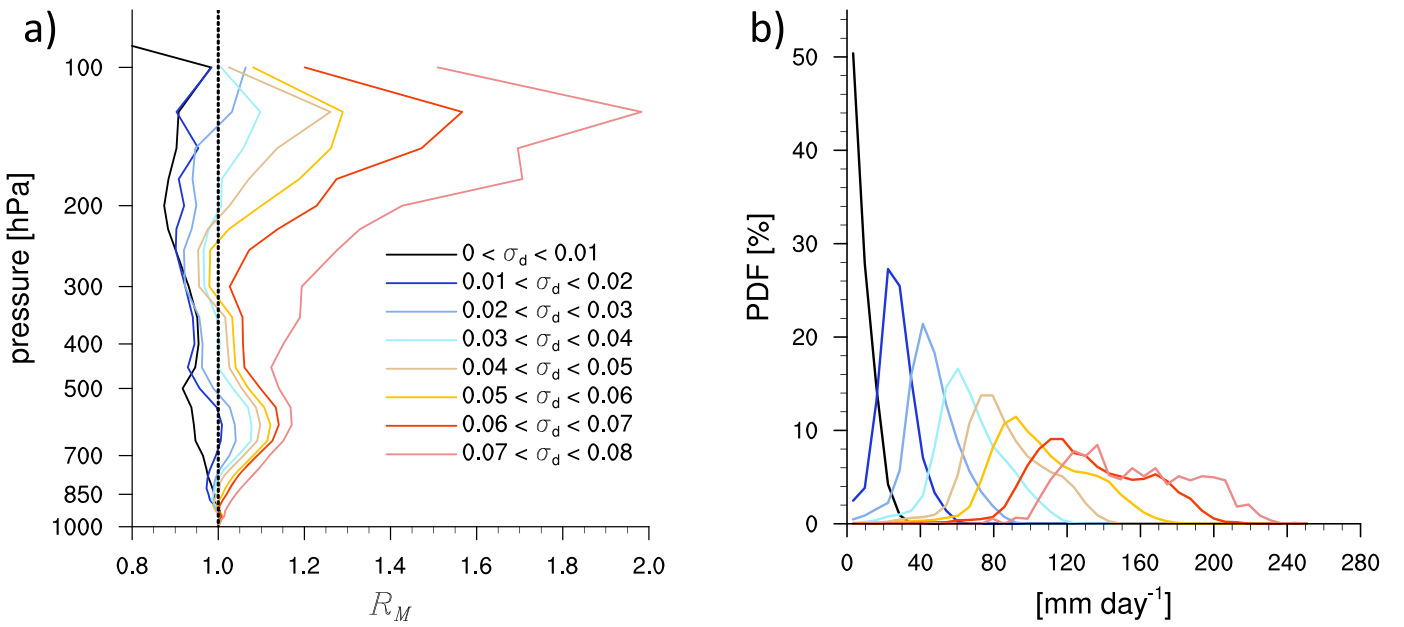


**Figure 11.** Convective behavior in E63-SMCM as sorted by SMCM-simulated values of $\sigma_d$ at the time step level. (a) Ratios $R_M$ between the actual mean convective updraft profiles per time step for each $\sigma_d$-bin and a hypothetical updraft profile obtained from linear scaling of the overall mean updraft mass-flux profile. Positive (negative) deviations from the reference line at $R_M = 1$ indicate larger (smaller) than linear scaling compared to the mean deep convective mass-flux profile per time step (see main text for details). (b) Average convective rain rate per time step (when present). All available time step data for January 2003 is used. The analysis is restricted to the inner tropics (23°N–23°S).

shown), because the atmospheric state at 500 hPa may suggest so. Midlevel convection is calculated in the majority of cases where deep convection is unsuccessful for $\sigma_d > 0$, followed by shallow convection, which makes up nonnegligible fractions of alternative convection for values of $\sigma_d < 0.03$.

For cases where $\sigma_d > 0$ and deep convection is calculated, updraft mass flux increases with $\sigma_d$ and the profiles $M_{\sigma_d}$ feature a pronounced maximum in low to midlevels (≈600 hPa) which compares favorable to observations [*Kumar et al.*, 2015, 2016, not shown]. The increase of updraft mass flux with $\sigma_d$ is straightforward to comprehend—but an important question to address would be whether or not this increase is linear in $\sigma_d$. We thus compute hypothetical mass-flux profiles for bins of $\sigma_d$ (width $\Delta\sigma_d$=0.01) $\hat{M}_{\sigma_d}$ by scaling the overall mean profile $\bar{M}$ such that $\hat{M}_{\sigma_d} = f_{\sigma_d}\bar{M}$, with $f_{\sigma_d} = \frac{M_{\sigma_d}}{\bar{M}}|_{1000\,\mathrm{hPa}}$. We show the ratio between the actual and hypothetical updraft mass-flux profiles $R_M = \frac{M_{\sigma_d}}{\hat{M}_{\sigma_d}}$ in Figure 11a. The updraft mass-flux profiles do not scale linearly with $\sigma_d$. However, deviations from a linear scaling are $\mathcal{O}(\pm 10\%)$ for the majority of cases (cf., counts per $\sigma_d$-bin in Figure 10) up to ≈ 250 hPa. Nonlinearity increases with $\sigma_d$ and positive deviations from linear scaling are most pronounced at ≈600 hPa and above ≈ 250 hPa. A likely reason for this increased nonlinearity with larger values of $\sigma_d$ is a reduced impact of turbulent entrainment on strong convective events compared to weaker ones. Convective rain rates per time step increase with $\sigma_d$, with the distribution getting wider for large $\sigma_d$ (Figure 11b). This increase in spread could be related to the large spread in the convective response given the environmental conditions (even for deterministic convection schemes, cf., *Watson et al.* [2015]) and the relatively small sample size for large values of $\sigma_d$.

We show total mass-flux characteristics of all convective types (deep, shallow, mid) of both model simulations in Figure 12. Overall, deep convection is substantially weaker in E63-SMCM compared to E63-REF (Figure 12a)—a feature related to the overall smaller values of $M_{cb}$ in E63-SMCM (Figure 12d). This is especially evident from the average instantaneous convective mass-flux profiles (Figure 12c). The mean deep convective mass-flux profile in E63-REF peaks at lower levels than in E63-SMCM (≈750 hPa versus ≈600 hPa) and this maximum is about 4 times higher than in E63-SMCM (Figure 12a). However, deep convection occurs more often at all levels in E63-SMCM (Figure 12b). Observations indicate that mean tropical deep convective mass-flux profiles peak around 5–6 km and that the PDF of $M_{cb}$-values should be approximately log-normally distributed due to their dependence on $\sigma_d$ [*Davies et al.*, 2013b; *Gottwald et al.*, 2016; *Kumar et al.*, 2015, 2016; *Dorrestijn et al.*, 2016]. E63-SMCM thus compares better to observations than E63-REF. This also holds for the magnitude of mean deep convective mass fluxes (Figure 12c), with the ones in E63-REF being

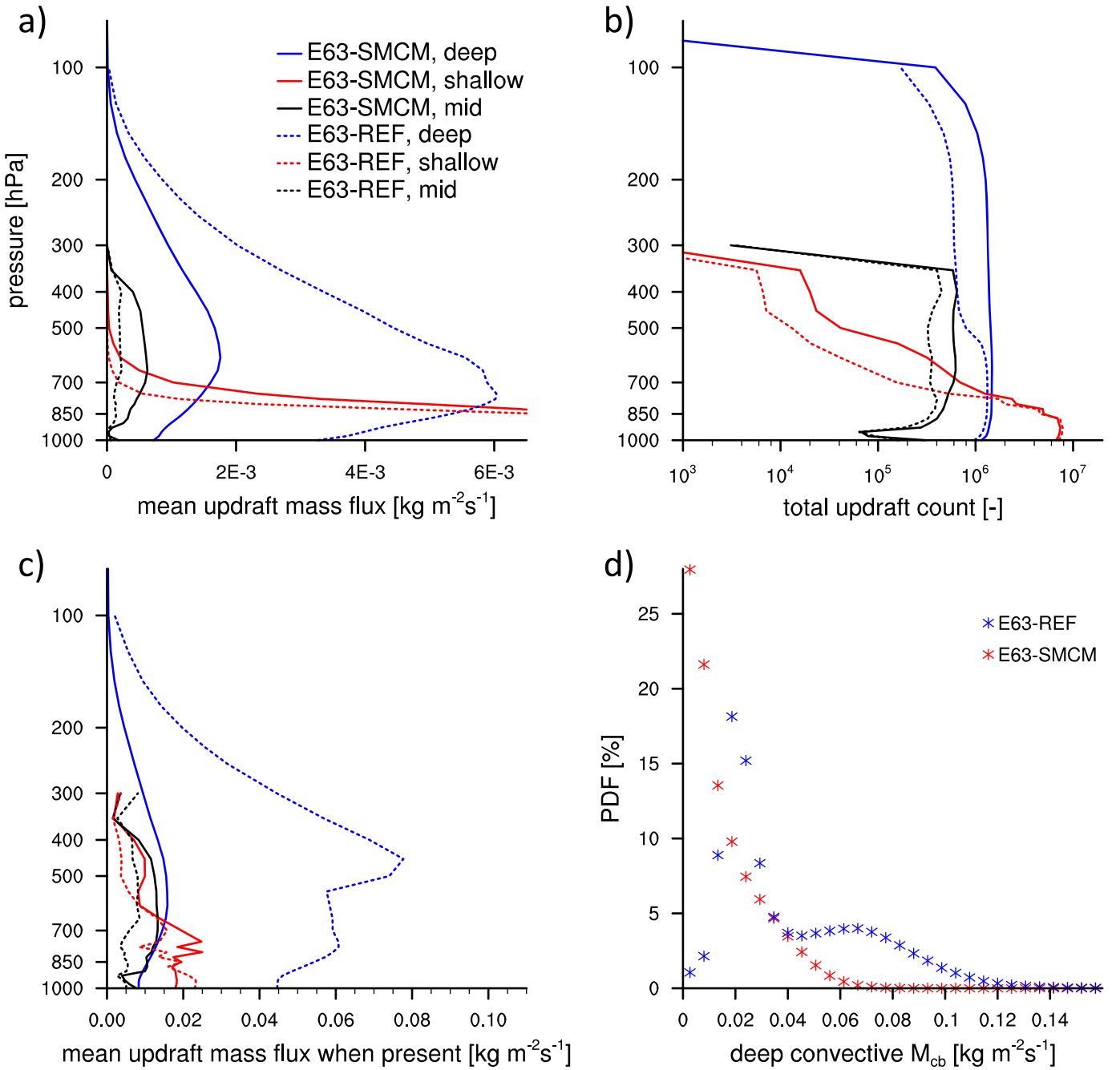


**Figure 12.** Convective mass-flux characteristics derived from time step data. All available time step data for January 2003 are used. The analysis is restricted to the inner tropics (23°N–23°S). (a) Average deep (blue), shallow (red), and mid (black) convective mass flux; (b) total updraft count per level per convective type; (c) updraft mass-flux per time step when present for the entire 31 day period and analysis region. Data shown for E63-REF (solid curves) and E63-SMCM (dashed curves); (d) PDF of deep convective cloud base mass flux $M_{cb}$ for simulations E63-REF (blue) and E63-SMCM (red).

substantially stronger than those derived from observations [*Kumar et al.*, 2016] (Figure 13). On the contrary, the mean deep convective mass fluxes in E63-SMCM (Figure 12c) compare very well to the observations.

Additionally, the number of deep convective updrafts in E63-REF decreases rather abruptly at altitudes between 600 and 500 hPa (Figure 12b). This aspect of the convection scheme was already pointed out by *Möbis and Stevens* [2012]. It results from the convection scheme performing deep convection in environments which do not support deep clouds (see below for further quantification).

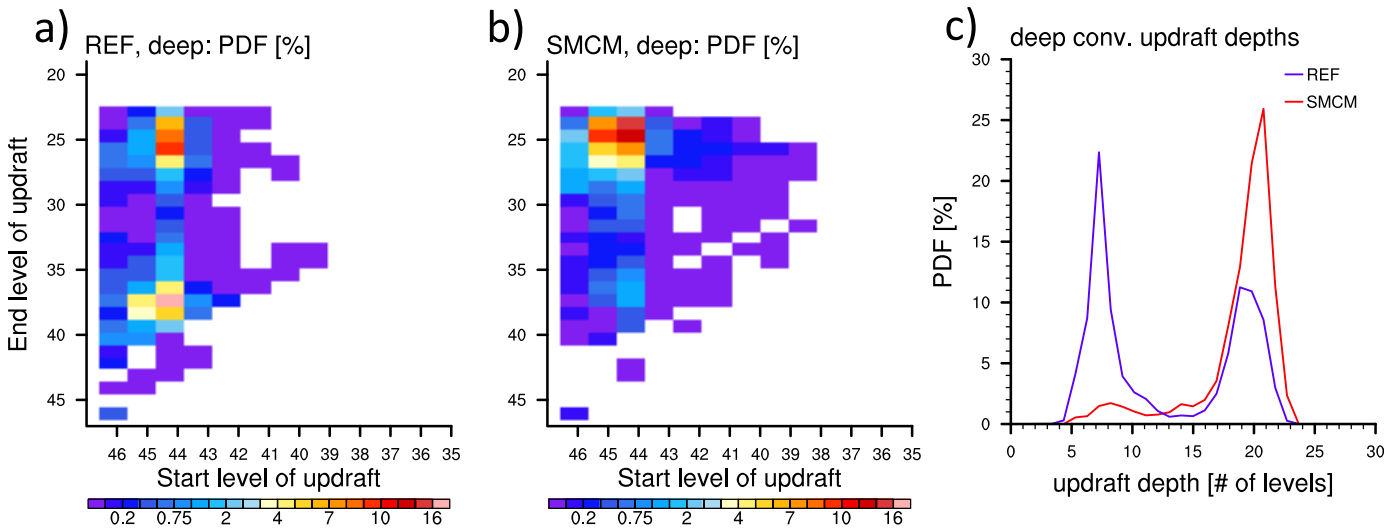


**Figure 13.** Deep convective updraft depth statistics. Joint PDFs of start model level of deep convective updraft versus end model level of deep convective updraft for simulations (a) E63-REF and (b) E63-SMCM. Model level 46 corresponds to the surface layer, level 25 is located at ≈200 hPa, and level 20 is located at ≈80 hPa. (c) The corresponding PDFs of deep convective updraft depths (E63-SMCM: red, E63-REF: blue). Note the nonlinear color scale for Figures 13a and 13b of 11 January 2003 is used. The analysis is restricted to the inner tropics (23°N–23°S).

To further illustrate the differences between the two versions of the convection scheme, we show statistics of deep convective updraft depths in the inner tropics (23°N-23°S) per time step for both simulations in Figure 13. We construct Figure 13 from time step data obtained for one day of simulation—the statistics are qualitatively similar for all days. For E63-SMCM, the majority of deep convective updrafts terminates in the upper troposphere (Figure 13b), which results in a more or less mono-modal distribution of updraft depths (Figure 13c). For E63-REF on the other hand, deep convective updrafts show two preferred termination regions: one in the lower-middle troposphere below ≈600 hPa (level ≈37) and the other in the upper troposphere (Figure 13a), leading to a pronounced bimodal distribution of deep convective updraft depths (Figure 13c).

Shallow convection in E63-SMCM is less intense in the boundary layer and more intense above ≈800 hPa compared to E63-REF (Figure 12a). Furthermore, shallow convection happens more often throughout the lower to middle troposphere in E63-SMCM (Figure 12b). Together with the deep convective behavior described above, this indicates that in E63-REF, many "deep convective" clouds can be interpreted as representing a congestus cloud mode which the deep convective part of the scheme is trying to represent. In contrast, in E63-SMCM, these clouds are now likely represented through the shallow convection scheme. Along with the reduction of deep convective mass flux, this results in an overall increase of mass-flux contribution by shallow convection, and the convective heating associated with it, in E63-SMCM. While deep convective heating dominates in E63-REF and projects on the first baroclinic mode, we hypothesize that the additional shallow heating in E63-SMCM likely excites the second baroclinic mode and could thus be the reason for the more realistic simulation of equatorial Kelvin waves [cf., *Wheeler et al.*, 2000; *Straub and Kiladis*, 2003 regarding the observed structure of convectively coupled Kelvin waves].

*Möbis and Stevens* [2012] already noted that the standard convection scheme often terminates the deep convective updraft at midlevels due to a dry midtroposphere, which actually renders the decision to perform deep convection at least physically questionable [e.g., *Derbyshire et al.*, 2004; *Del Genio*, 2012]. The SMCM on the other hand does not favor the presence of deep convection if the middle troposphere is dry or in subsiding regimes (cf., section 2.1). In fact, the original deep-shallow-trigger is mostly inconsistent with the SMCM—the majority of "deep" events according to the deep shallow trigger actually show $\sigma_d = 0$ and are thus changed to "shallow" (over land and ocean, not shown).

Congestus clouds are typically much smaller than their deep convective counterparts. Turbulent entrainment rates in cumulus convection are commonly assumed proportional to the inverse cloud radius. As the entrainment rate used for computing shallow convection in ECHAM6.3's convection scheme is significantly higher than that used for deep convection, the representation of congestus clouds by the shallow

convection scheme in E63-SMCM is likely favorable to their representation by the deep scheme in E63-REF. However, neither solution is ideal. The original SMCM [*Khouider et al*., 2010] contains congestus clouds as a separate cloud type and work is underway to introduce area fractions for congestus in the SMCM implementation of ECHAM.

The spatial distribution of deep convective events is substantially different between the simulations. In Figure 14 we show the spatial distribution of the amount of time steps in which deep convection is calculated for a given day (2 January 2003, results are qualitatively similar for all days)—unfiltered (Figures 14a and 14c) and filtered for occasions in which the resulting deep convective updraft has a depth of more than 15 model levels (Figures 14b and 14d). Total precipitation on daily timescales matches well with the distribution of convective events displayed in Figures 14a and 14c (not shown). Filtering for occasions in which deep convection actually goes deep yields a substantially different distribution of deep convective events in E63-REF compared to the unfiltered data (Figures 14a and 14b). For E63-SMCM, the distributions are very similar for the filtered and unfiltered data (Figures 14cand 14d). This is to be expected given the previous analysis of deep convective updraft depth (Figure 13). While tropical deep convection in E63-SMCM appears to be largely organized in propagating clusters (Figures 14c and 14d, cf., Figures 5 and 6b) with continuous convection over the course of 1 day, the picture looks quite different for E63-REF (Figures 14a and 14b). In that simulation, tropical convection is much more spatially homogeneous over the whole tropics (Figure 14a) and already somewhat resembles the mean structure of the ITCZ on daily timescales. Filtering for genuine deep convection also indicates that these events are not nearly as persistent and structured as the clusters simulated in E63-SMCM (Figure 14b).

Observations of tropical precipitation at daily timescales show a spatial structure comparable to that simulated by E63-SMCM [e.g., *Huffman et al*., 2001]: propagating precipitation clusters with dry areas between them. This is consistent with the Hovmöller diagrams in Figure 5 and the lag-autocorrelation analysis of mean daily total precipitation $\alpha_p(\tau)$ (Figure 6). The daily distribution of convection as simulated in E63-REF is inconsistent with observations (both spatially and temporally, cf., Figures 5 and 6) in the sense that it is not as organized and intermittent on large scales as is observed (cf. Figure 5). We can now clearly associate this behavior with the more frequent but spatially more organized diagnosis of deep convection in E63-SMCM.

One reason for the increased convective organization in E63-SMCM could be the increased sensitivity to free tropospheric humidity compared to E63-REF. By now, multiple studies have shown that increasing a convection schemes' sensitivity to free tropospheric moisture leads to a better simulation of the MJO [e.g., *Kim et al*., 2011; *Del Genio et al*., 2012; *Hirons et al*., 2013a; *Klingaman and Woolnough*, 2014; *Hannah and Maloney*, 2014; *Zhu and Hendon*, 2015].

To quantify the simulated relationship between atmospheric moisture and convection in our simulations, we construct composite vertical profiles of daily mean relative humidity (RH) as a function of daily mean precipitation as seen in reanalysis/observation and the two model simulations in Figure 15. In the reanalysis (Figure 15a), tropospheric moisture gradually increases with precipitation, with the occurrence of weak precipitation associated with a substantially drier middle troposphere than high precipitation. For high precipitation, the entire troposphere exhibits values of RH $>$90%, in agreement with the known relationship between precipitation and column integrated water vapor [*Bretherton et al*., 2004; *Holloway and Neelin*, 2009]. Both model simulations show a RH-precipitation relationship similar to one another and to observations for weak precipitation (Figures 15b and 15c)—but the boundary layer is too wet and the middle troposphere is too dry compared to observations, respectively. For high precipitation events, the two model simulations show pronounced differences. E63-REF features a gradual drying of the boundary layer with increasing precipitation and a relatively dry region in the lower to middle troposphere which persists even for the highest precipitation rates. E63-SMCM compares better to observations, especially for environments favoring high precipitation. However, E63-SMCM is moister than the reanalysis between 600 and 800 hPa for intermediate precipitation and shows a too moist boundary layer throughout, somewhat overcompensating the errors of E63-REF compared to the reanalysis.

It is well known that capturing the observed RH-precipitation relationship is crucial for a GCM to feature an adequate representation of TISV [e.g., *Thayer-Calder and Randall*, 2009; *Kim et al*., 2009, 2011; *Del Genio et al*., 2012; *Hirons et al*., 2013b]. Capturing the observed RH-precipitation relationship could therefore contribute to the improved MJO in E63-SMCM compared to the standard model. However, the analysis of *Klingaman et al*. [2015], exploiting data from multiple GCMs obtained in the framework of a model intercomparison

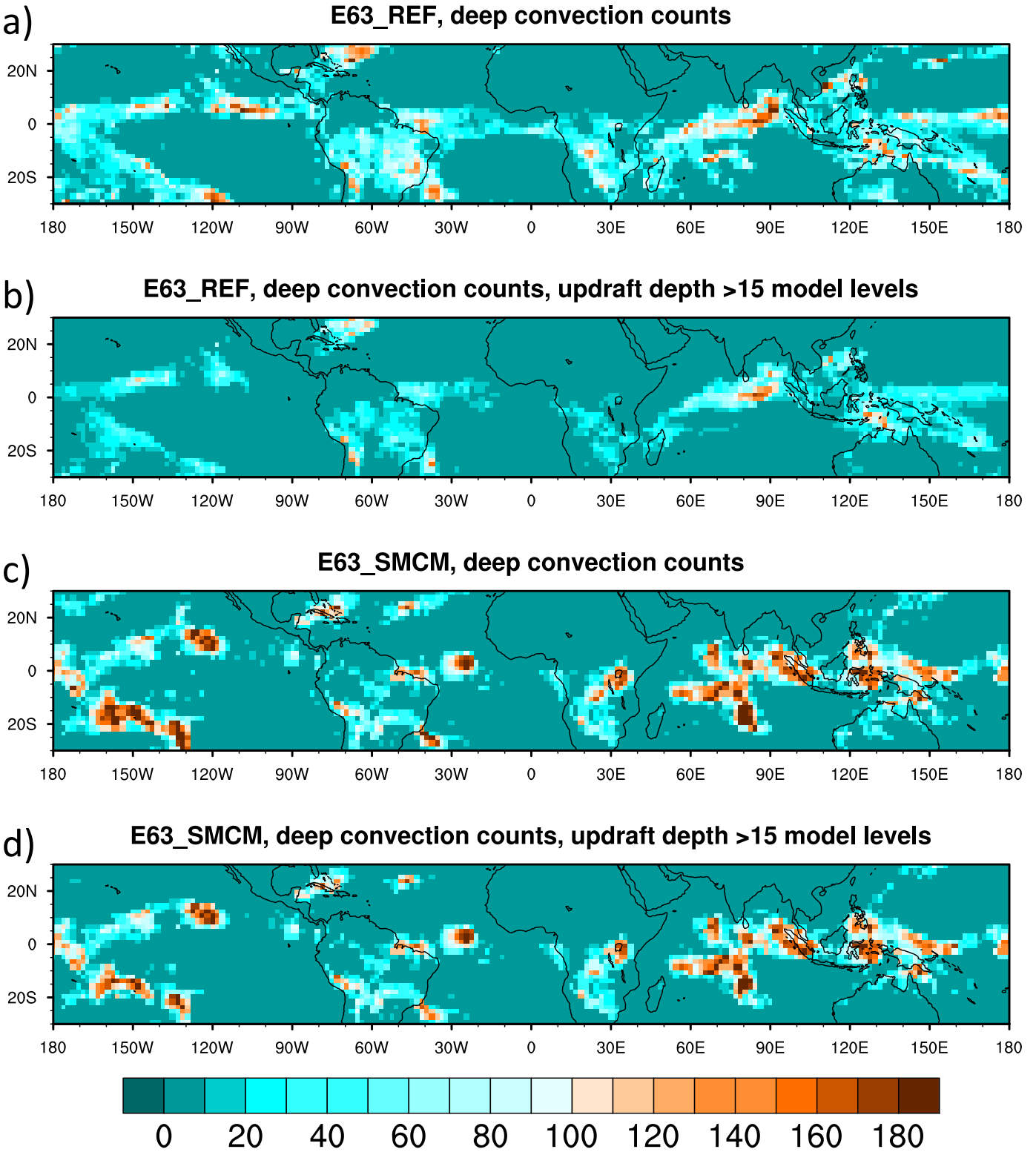


**Figure 14.** Number of time steps in which deep convection is calculated on a particular day (2 January 2003) in simulations (a and b) E63-REF and (c and d) E63-SMCM. Figures 14a and 14c show all instances where deep convection is calculated, Figures 14b and 14d show only instances where the resulting deep convective updraft is deeper than 15 model levels. There are 192 time steps per day (7.5 min time step).

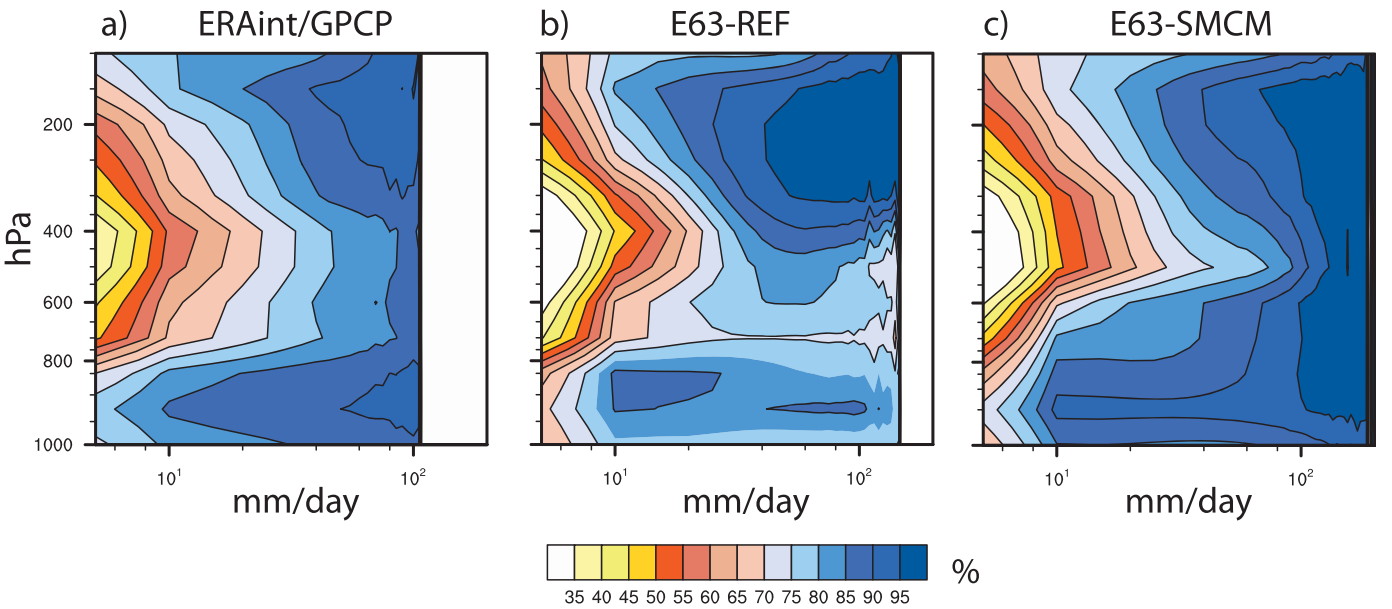


**Figure 15.** Composite vertical profiles of daily mean relative humidity versus precipitation for the inner tropics (23°N–23°S). (a) Observations (ERA-Interim and GPCP), (b) E63-REF, and (c) E63-SMCM. Only profiles constructed from more than 50 samples are plotted.

project targeted at understanding diabatic processes of the MJO, revealed no link between a model's fidelity to represent the MJO and its RH-precipitation relationship. We explore this further in the context of our implementation of the SMCM into ECHAM6.3 in section 5.

There are two mechanisms at work improving upon the representation of the RH-precipitation relationship when the SMCM is incorporated into ECHAM's convection scheme. The first mechanism simply relates to the direct dependence of deep convection on mid-tropospheric humidity in the SMCM, which inhibits the formation of deep convection if the middle troposphere is dry [*Khouider et al.*, 2010 and section 2]. The second mechanism is related to the modified closure of the convection scheme. The observation-trained closure [*Peters et al.*, 2013] gives a more realistic relation between the model large-scale state and deep convective cloud base mass flux. This results in substantially weaker convective mass fluxes in E63-SMCM compared to E63-REF (Figure 12). By having a weaker mass flux, the convective drying per time step will be smaller and the balance between large-scale moistening and convective drying at deep convective points will shift to more moistening/less drying. Thus, deep convection persists longer on a time step to time step basis (Figure 14) in order to remove a convective instability. As a result, convection persists in high humidity environments, leading to an improved RH-precipitation relationship in E63-SMCM compared to E63-REF. We investigate this connection further in the section 5.

Recent studies have shed light on the role of large-scale, or "stratiform," diabatic heating in creating and maintaining MJO-like features in the tropics. As stratiform heating contributes strongly to the top-heavy heating profile in the MJO [*Lin et al.*, 2004], representing this heating correctly in GCMs may be important to improve MJO-simulation in such models. Along those lines, *Crueger and Stevens* [2015] found that stratiform cloud longwave radiative effects act to enhance the stratiform diabatic heating profile in the tropics resulting in a slowdown of the eastward propagation of the MJO. *Deng et al.* [2016] found that incorporating heating associated with stratiform precipitation processes has the same result. In E63-SMCM large-scale precipitation is more closely associated with convective precipitation on multiday timescales compared to E63-REF (Figure 16). This could be another reason for the improved representation of CCEW's and the MJO in E63-SMCM compared to E63-REF. This is also further investigated in section 5.

## 5. Discussion

We have shown that our implementation of the SMCM into ECHAM6.3 leads to improved simulation of the MJO and CCEW's. These improvements may be the result, or combination, of the improved precipitation-

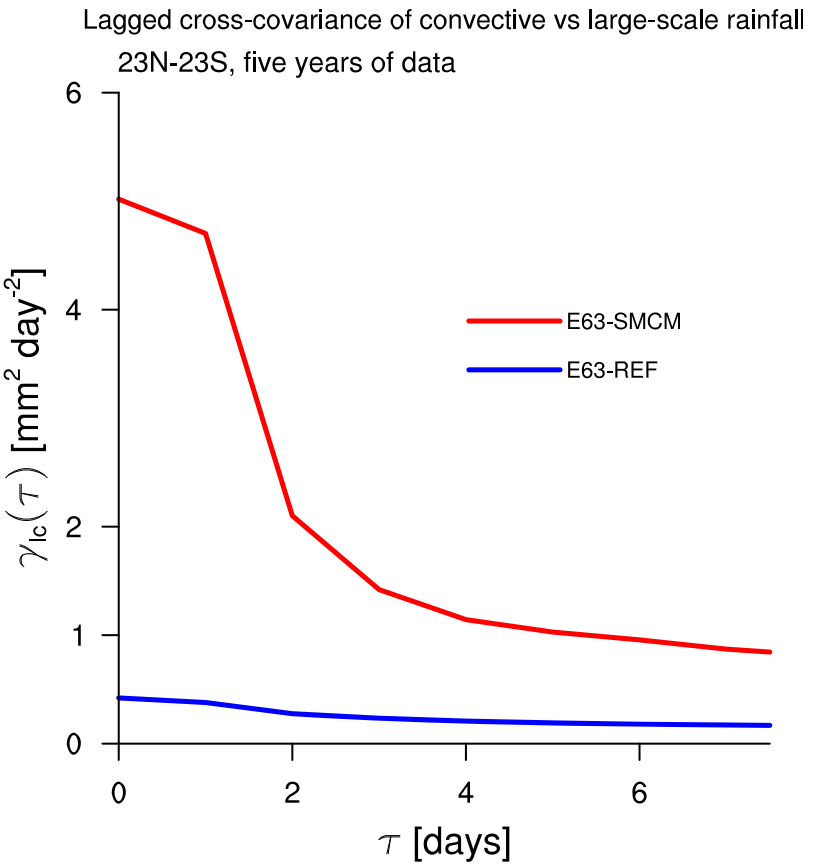


**Figure 16.** Mean lagged cross-covariance $\gamma_{lc}(\tau)$ of daily mean large-scale precipitation versus convective precipitation in the tropics (23°N–23°S) at the model grid box scale in simulations E63-SMCM (red) and E63-REF (blue). Five years of data are used (1979–1983).

moisture coupling, the improved spatiotemporal coherence of tropical convection on daily timescales, more continuous deep convection on subdaily timescales and the increased cross covariance of simulated convective and large-scale precipitation.

To isolate the prime factors determining the improvements in the simulation of tropical daily and intraseasonal variability in ECHAM6.3, we have performed a suite of sensitivity experiments (cf., Table 1). We designed the sensitivity experiments in such a way that we sample two main aspects of our implementation, namely the reduction of deep convective mass fluxes and the incorporation of stochasticity in E63-SMCM compared to E63-REF. This approach assumes that these two aspects project onto the changes in model behavior described in the preceding paragraph. Regarding the first aspect, we aimed at devising model setups in which deep convective mass fluxes are as similar as possible between the two versions of the convection scheme. We therefore increased $w_{cb}$ from 1 to 3 m s$^{-1}$ for the SMCM setup using $n = 20$ ("E63-SMCM, n20w3") and increased the CAPE timescale $\tau_{\mathrm{CAPE}}$ from 2 to 4 and 8 h for the standard setup ("E63-REF, $\tau_{\mathrm{CAPE}}$=4(8)h"). Although we did not obtain a perfect match of the simulated deep convective mass fluxes between the two model versions, they are significantly closer than using the standard setups described earlier in this paper (supporting information Figure S4). Regarding the second aspect, we performed simulations using $n$=10(40), combined with $\omega_{cb}$=1 m s$^{-1}$ in the SMCM setup ("E63-SMCM, n1(4)0w1"). The sensitivity experiments were each run for a period of 13 years (1978–1990) with the first year considered as spin-up and the remaining 12 being used for analysis. Each sensitivity experiment was also run with time step output for January 2003 after one year of spin-up. A detailed discussion of the sensitivity experiments is provided in the supporting information.

We summarize the capacity of each model setup to simulate the MJO, as measured by the objective MJO-Index of *Crueger et al.* [2013] (equation (6)), by devising simple metrics capturing model behavior deemed potentially important for simulating the MJO in a GCM. These metrics are:

**Table 1.** Summary of Experiment Setups for the Sensitivity Experiments

| Experiment | Specifications $n$ | $w_{cb}$ (m s$^{-1}$) | $\tau_{CAPE}$ (h) |
|---|---|---|---|
| E63-REF | n/a | n/a | 2 |
| E63-SMCM | 20 | 1 | n/a |
| E63-SMCM, n10w1 | 10 | 1 | n/a |
| E63-SMCM, n40,w1 | 40 | 1 | n/a |
| E63-SMCM, n20,w3 | 20 | 3 | n/a |
| E63-REF, $\tau_{CAPE}=4h$ | n/a | n/a | 4 |
| E63-REF, $\tau_{CAPE}=8$ h | n/a | n/a | 8 |

1. Relative humidity averaged over 700–500 hPa for daily mean precipitation rates >80 mm d$^{-1}$. This metric is derived from data used to produce the composite profiles in supporting information Figure S6. This metric sheds light on the established conjecture that a realistic representation of the RH-precipitation relationship is important for MJO simulation [*Kim et al*., 2011, 2012; *Del Genio et al*., 2012; *Hirons et al*., 2013a; *Klingaman and Woolnough*, 2014; *Hannah and Maloney*, 2014; *Zhu and Hendon*, 2015; *Crueger and Stevens*, 2015], with the results of *Klingaman et al*. [2015] challenging this established view. This metric also captures the effect of reduced/increased deep convective mass fluxes—a reduction of convective mass flux in the original ECHAM6.3 convection scheme improves the RH-precipitation relationship whereas an increase in convective mass flux in the SMCM setup deteriorates the RH-precipitation relationship (supporting information Figure S6).
2. Lag autocorrelation of daily mean rainfall in the tropics $\alpha_{p,d}(\tau)$ at the model grid scale at $\tau = 1$ day (Figure 6a and supporting information Figure S5a). This metric tests whether representation of the spatio-temporal coherence of tropical rainfall on daily timescales (Figure 6a) is important for capturing the MJO in ECHAM6.3.
3. Lag autocorrelation of time step rainfall in the tropics $\alpha_{p,ts}(\tau)$ at the model grid scale for $\tau = 6$ h (Figure 6b and supporting information Figure S5b). This metric addresses whether the variability of deep convection on subdaily timescales is important for capturing the MJO in ECHAM6.3. For the SMCM setup, this tests whether the incorporation of convective memory at the grid scale is important.
4. Lag cross covariance of convective and large-scale daily mean rainfall in the tropics $\gamma_{lc}(\tau)$ at the model grid scale for $\tau = 1$ day (Figure 16 and supporting information Figure S5c). This metric addresses the conjecture that a close relationship between convective and large-scale rainfall in the tropics—which results in a more realistic top-heavy diabatic heating profile—is important for simulating the MJO [*Crueger and Stevens*, 2015; *Deng et al*., 2016]. Again, the results of *Klingaman et al*. [2015] challenge this view.

The above metrics and the associated values of the MJO-Index are displayed in Figure 17. With the standard convection scheme, the indices range from 0 to 0.08, whereas they range from 0.22 to 0.36 for the SMCM setup. These ranges are within the range of uncertainty estimated from GCM ensemble simulations [*Crueger et al*., 2013, Figure 9], implying that each version of the convection scheme shows a similar capacity to simulate the MJO irrespective of the applied sensitivity test. Even for the SMCM setup, these values are significantly lower than those derived from reanalysis data, indicating that the MJO signal in all model setups remains too weak (cf., Figure 8). In order for one of the above metrics to indicate model behavior important for MJO simulation, its value should not depend on the applied sensitivity test and maybe even show values close to the ones derived from observations (when available).

It is clear that capturing the observed moisture-precipitation relationship is not key to simulating a realistic MJO in ECHAM6.3 (Figure 17a, in agreement with *Klingaman et al*. [2015]). Especially for the standard convection scheme, this metric spans a wide range of values with no impact on MJO skill. The same holds for the SMCM setup where the middle troposphere is drier in the simulation with increased $w_{cb}$—the choice of $n$ has close to no impact on the metric's value. This metric also nicely illustrates that a reduction in deep convective mass flux in either convection scheme leads to an improved RH-precipitation relationship compared to observations, i.e., high rain rates are simulated in environments featuring a moist middle troposphere.

The incorporation of short-term memory also does not seem to play a role (Figure 17c) as there is substantial spread among the model simulations for this metric, e.g., $\alpha_{p,ts}(6\,\mathrm{h})$ ranges from about 0.15–0.3 in the SMCM setup, but the simulated MJO is practically identical. The same holds for the sensitivity tests with the standard convection scheme where $\alpha_{p,ts}(6\,\mathrm{h})$ ranges from about 0.08–0.25. Reducing the deep convective mass fluxes leads to more continuous surface rainfall over the course of 6 h in both versions of the convection scheme.

For the metric illustrating the importance of cross covariance of convective and large-scale daily mean rainfall (Figure 17d), the values cluster closely at small values for the E63-REF setups. For the E63-SMCM setups, the

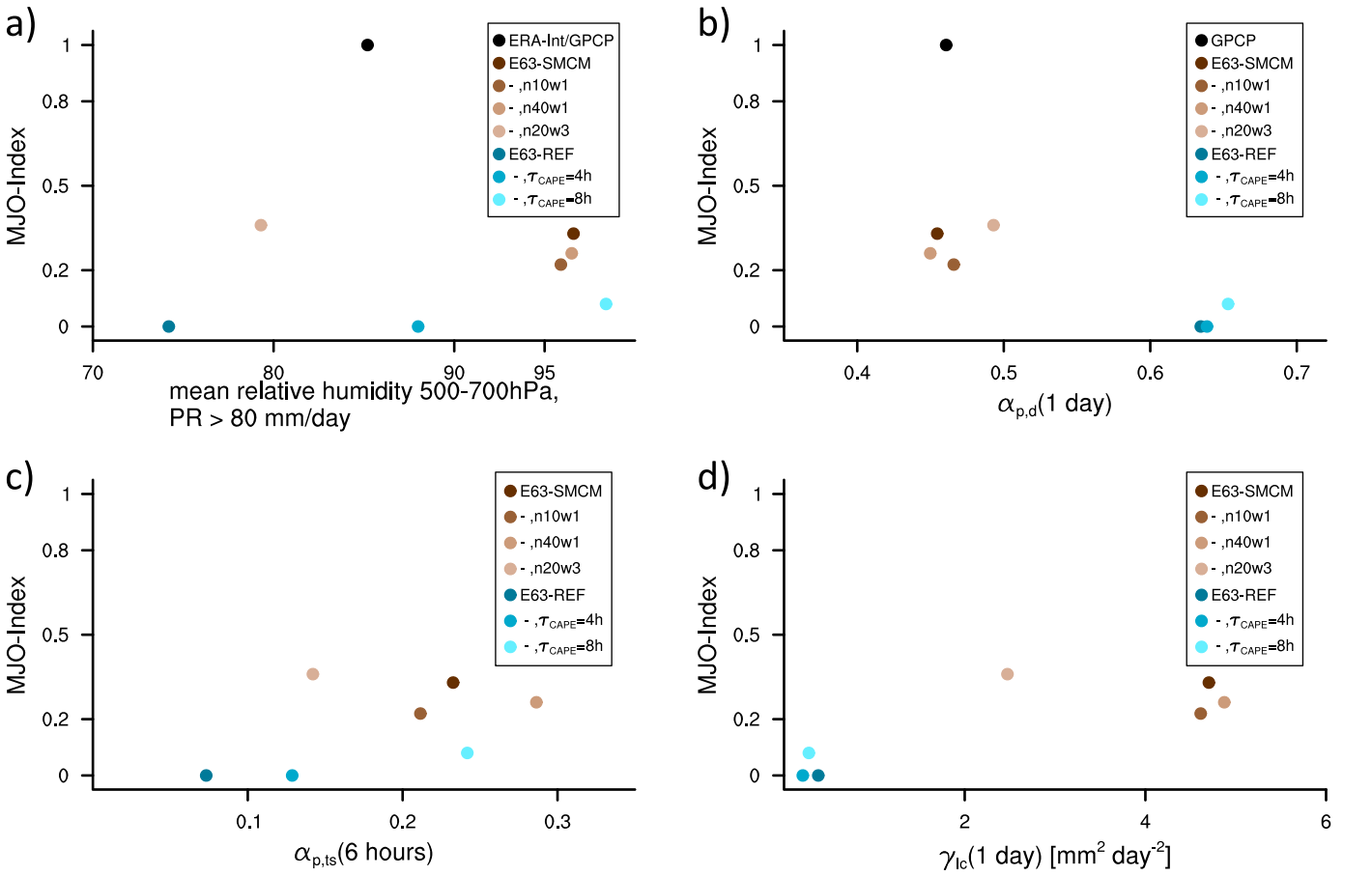


**Figure 17.** MJO-Index as defined by *Crueger et al.* [2013] as function of metrics derived from observations and model simulations: (a) 500–700 hPa average relative humidity for bins of daily mean rainfall $>80\,\frac{mm}{day}$, (b) lag-autocorrelation of daily mean total rainfall after 1 day, (c) lag-autocorrelation of time step total precipitation after 6 h, and (d) lag-cross-covariance of large-scale versus convective daily mean rainfall after 1 day. More details on the sensitivity experiments are provided in supporting information Text S2, Figures S1–S7, and Table S2.

values cluster at much higher values except for the simulation with increased $w_{cb}$ which lies in between the REF and the SMCM setups. We can thus not fully rule out the possibility that a close relationship between simulated convective and large-scale precipitation has a positive impact on MJO simulation in ECHAM6.3.

The only parameter with a very clear signal on MJO performance is the lag-autocorrelation of daily mean rainfall (Figure 17b). It is worth noting that the values of $\alpha_{p,d}$ (1 day) for the SMCM setups (0.45–0.49) all cluster around the observed value (0.46), while the values for the REF setups cluster around values of 0.65. It is also apparent that the spatiotemporal coherence of tropical rainfall depends strongly on the convection scheme rather than its parameters. In other words, it is an intrinsic characteristic of the convection scheme itself.

For the SMCM setup as illustrated in this study, the coupling of the occurrence of deep convection to large-scale vertical velocity $\omega_{500}$ will be most effective in generating the simulated spatiotemporal coherence of daily mean rainfall in the tropics. On the one hand, this coupling suppresses deep convection in subsiding environments. On the other hand, midlevel ascending motion will effectively trigger deep convection—comparable to the convective triggering mechanism proposed in *Yang and Ingersoll* [2013] in which gravity wave induced geopotential perturbations trigger convection which then evolves into convective clusters and forms the basis for MJO-like disturbances.

## 6. Conclusions

We have implemented a modified version of the Stochastic Multicloud Model (SMCM) [*Khouider et al.*, 2010] into the convection parameterization of the state-of-the-art global climate model ECHAM6.3. The employed

setup of the SMCM is based on the results presented in *Peters et al*. [2013] and couples the occurrence and strength of deep convection in ECHAM6.3 to vertical velocity and relative humidity at 500 hPa—contrary to the standard convective trigger in ECHAM6.3 [cf., *Möbis and Stevens*, 2012] with the standard CAPE closure [*Nordeng*, 1994]. The implemented SMCM-based closure of the convection scheme therefore provides observations informed relationships between the large-scale environment and the deep convective cloud base mass flux. We deliberately kept the implementation of the SMCM into ECHAM6.3 as simple as possible as we consider this work as a proof-of-concept to motivate further efforts in improving the representation of convection through the implementation of the ideas contained in the SMCM.

We ran 30 year AMIP simulations (1979–2008) with the modified version of ECHAM6.3, E63-SMCM, and the standard model setup, E63-REF. Compared to E63-REF, E63-SMCM improves upon the simulation of tropical intraseasonal variability (TISV), including but not limited to the MJO, with limited changes to the simulated mean climate.

Interestingly, although having chosen a different implementation strategy of the SMCM into a comprehensive GCM (CFSv2), *Goswami et al*. [2016] find very similar improvements in terms of simulated tropical synoptic and intraseasonal variability.

We performed an in-depth analysis of the behavior of the two convection representations to distil the prime model characteristics resulting in the improved capacity of E63-SMCM to simulate TISV compared to E63-REF. From those two simulations alone, multiple factors could have contributed to the improvements in the SMCM setup: improved (i) moisture-convection coupling, (ii) spatiotemporal coherence of tropical rainfall on daily timescales, (iii) representation of deep convective mass fluxes (all compared to observations), (iv) increased covariance of simulated convective and large-scale rainfall, and (v) more continuous deep convection on subdaily timescales.

Additional sensitivity experiments lead us to the conclusion that it is the more realistic representation of the spatiotemporal coherence of tropical rainfall on daily timescales which contributes most to the improved capacity of E63-SMCM to simulate the MJO. This is because the SMCM does not allow for deep convection to occur in environments which do not support deep convection, i.e., subsidence regimes and/or occasions where the middle troposphere is dry. This results in zonally propagating precipitation clusters in the tropics with extended non-precipitating regions between them—a behavior effectively suppressing the common drizzle problem in current generation GCMs [e.g., *Stephens et al*., 2010]. Further, we found that the simulated spatiotemporal coherence of tropical rainfall is independent of the strength of the deep convective mass fluxes (E63-REF and E63-SMCM) or the stochasticity of the SMCM setup. It is therefore an intrinsic property of the convection scheme itself and not of its parameters.

The improved moisture convection coupling found in E63-SMCM compared to E63-REF results from the reduced deep convective mass flux per time step in E63-SMCM. Reducing the deep convective mass flux of the operational ECHAM6.3 convection scheme shifts the moisture-precipitation relationship towards the observed one—but this has no impact on the simulation of the MJO. Our results confirm the conclusions drawn in *Klingaman et al*. [2015] that correctly capturing the observed moisture precipitation relationship in a GCM does not guarantee an adequate simulation of TISV and the MJO in particular.

The incorporation of convective memory at the grid scale leads to more continuous precipitation in E63-SMCM on subhourly and hourly timescales compared to E63-REF. Precipitation in ECHAM6.3 also becomes more continuous on hourly timescales using the standard convection scheme by reducing the deep convective mass fluxes. This has no impact on simulated MJO, though. Detrimental influence of the large time step to time step variability in the standard scheme (Figure 6b) cannot be ruled out.

We can also not fully rule out the effect of cross-covariance of simulated large-scale and convective precipitation $\gamma_{lc}$ on the simulation of the MJO in ECHAM6.3. $\gamma_{lc}$ is substantially larger in E63-SMCM compared to E63-REF, but is halved when the deep convective cloud base mass flux $M_{cb}$ is increased by a factor of three in E63-SMCM—with no effect on the simulated MJO.

Different degrees of stochasticity of the SMCM, investigated by changing the number of SMCM lattice points $n \times n$, modify the overall variability of deep convection in the tropics, but do not have an impact on simulated TISV and MJO in particular (contrary to the results of *Deng et al*. [2015] cf., supporting information).

Regarding the improved simulation of convectively coupled Kelvin waves in E63-SMCM compared to E63-REF, we hypothesize that the additional shallow convective heating in E63-SMCM likely excites the second baroclinic mode and could thus be the reason for the more realistic simulation of equatorial Kelvin waves [cf., *Wheeler et al*., 2000; *Straub and Kiladis*, 2003 regarding the observed structure of convectively coupled Kelvin waves].

In conclusion, we have shown that the SMCM can serve as integral building block for future convection schemes, with its positive impacts on the simulation of spatiotemporal coherence of tropical precipitation—and the associated improvements in simulating the MJO—standing out. We have mentioned some apparent failures of the scheme, like the missing link to land surface processes which lead to severe underestimation of rainfall over tropical land areas, especially the Amazon and the Maritime Continent. It was out of scope for this study to also couple the other two SMCM cloud types (congestus and stratiform) to ECHAM6.3. These issues are currently being approached. Together with the insights gained regarding ingredients needed for an improved simulation of TISV and the MJO in particular, we see the present study as an important contribution to the atmospheric science communities' dire need for an increased capacity in understanding and simulating processes related to atmospheric convection and its effects on the climate system [*Bony et al*., 2015].

**Acknowledgments**

We thank Mirjana Sakradzija and two anonymous reviewers for constructive comments on earlier versions of the manuscript and Robert Pincus for his supportive role as editor during the review process. We thank Norbert Noreiks and Bettina Diallo from the graphics team at MPI-M for assisting in creating adequate figures. K.P. acknowledges funding by the Australian Research Council within the Centre of Excellence for Climate System Science (CE110001028) and Deutscher Wetterdienst (DWD) within the Hans-Ertel-Zentrum for Weather Research (HErZ). T.C. acknowledges funding from the Cluster of Excellence "CliSAP" (EXC177) of Hamburg funded through the German Science Foundation (DFG). The model simulations were performed at the German Computing Centre for Climate and Earth System Research (Deutsches Klimarechenzentrum, DKRZ). Computing time was granted within the European Union Cloud Intercomparison, Process Study & Evaluation (EUCLIPSE) Project. The GPCP combined precipitation data were developed and computed by the NASA/Goddard Space Flight Center's Laboratory for Atmospheres as a contribution to the GEWEX Global Precipitation Climatology Project. GPCP data are hosted at the Integrated Climate Data Center (ICDC) at the University of Hamburg and were downloaded from there. AVHRR-OLR were provided by the National Oceanic and Atmospheric Administration (NOAA)-Cooperative Institute for Research in Environmental Sciences (CIRES) Earth System Research Laboratory (ESRL)/Physical Sciences Division (PSD) Climate Diagnostics Branch, Boulder, Colorado (http://www.cdc.noaa.gov). ERA-interim data sets are available from ECMWF (http://apps.ecmwf.int/datasets/data/interim-full-daily/). We thank Boualem Khouider for providing the original code of the SMCM, which we have adopted to run within a GCM environment. The figures were created using the NCAR Command Language (Version 6.2.1) [Software] (2014). Boulder, Colorado: UCAR/NCAR/CISL/VETS, https://doi.org/10.506/D6WD3XH5. Primary data and scripts used in the analysis and other supporting information that may be useful in reproducing the author's work are archived by the Max Planck Institute for Meteorology and can be obtained by contacting publications@mpimet.mpg.de.

## References

Adler, R. F., et al. (2003), The version-2 global precipitation climatology project (GPCP) monthly precipitation analysis (1979-present), *J. Hydrometeorol.*, *4*(6), 1147–1167.

Arakawa, A., and C.-M. Wu (2013), A unified representation of deep moist convection in numerical modeling of the atmosphere. Part I, *J. Atmos. Sci.*, *70*(7), 1977–1992, doi:10.1175/JAS-D-12-0330.1.

Bony, S., et al. (2015), Clouds, circulation and climate sensitivity, *Nat. Geosci.*, *8*, 261–268, doi:10.1038/ngeo2398.

Brenowitz, N. D., Y. Frenkel, and A. J. Majda (2015), Enhanced persistence of equatorial waves via convergence coupling in the stochastic multicloud model, *J. Atmos. Sci.*, *72*, 4701–4720, doi:10.1175/JAS-D-15-0135.1.

Bretherton, C., M. Peters, and L. Back (2004), Relationships between water vapor path and precipitation over the tropical oceans, *J. Clim.*, *17*(7), 1517–1528.

Crueger, T., and B. Stevens (2015), The effect of atmospheric radiative heating by clouds on the Madden-Julian Oscillation, *J. Adv. Model. Earth Syst.*, *7*, 854–864, doi:10.1002/2015MS000434.

Crueger, T., B. Stevens, and R. Brokopf (2013), The Madden-Julian oscillation in ECHAM6 and the introduction of an objective MJO metric, *J. Clim.*, *26*(10), 3241–3257, doi:10.1175/JCLI-D-12-00413.1.

Davies, L., et al. (2013a), A single-column model ensemble approach applied to the TWP-ICE experiment, *J. Geophys. Res. Atmos.*, *118*, 6544–6563, doi:10.1002/jgrd.50450.

Davies, L., C. Jakob, P. May, V. V. Kumar, and S. Xie (2013b), Relationships between the large-scale atmosphere and the small-scale convective state for Darwin, Australia, *J. Geophys. Res. Atmos.*, *118*, 11,534–11,545, doi:10.1002/jgrd.50645.

De La Chevrotière, M., B. Khouider, and A. J. Majda (2014), Calibration of the stochastic multicloud model using Bayesian inference, *SIAM J. Sci. Comput.*, *36*(3), B538–B560, doi:10.1137/13094267X.

De La Chevrotière, M., B. Khouider, and A. J. Majda (2016), Stochasticity of convection in giga-les data, *Clim. Dyn.*, *47*(5), 1845–1861, doi:10.1007/s00382-015-2936-z.

Dee, D. P., et al. (2011), The ERA-Interim reanalysis: Configuration and performance of the data assimilation system, *Q. J. R. Meteorol. Soc.*, *137*(656), 553–597, doi:10.1002/qj.828.

Del Genio, A. D. (2012), Representing the sensitivity of convective cloud systems to tropospheric humidity in general circulation models, *Surv. Geophys.*, *33*(3–4), 637–656, doi:10.1007/s10712-011-9148-9.

Del Genio, A. D., Y. Chen, D. Kim, and M.-S. Yao (2012), The MJO transition from shallow to deep convection in CloudSat/CALIPSO data and GISS GCM simulations, *J. Clim.*, *25*(11), 3755–3770.

Deng, Q., B. Khouider, and A. J. Majda (2015), The MJO in a coarse-resolution GCM with a stochastic multicloud parameterization, *J. Atmos. Sci.*, *72*(1), 55–74.

Deng, Q., B. Khouider, A. J. Majda, and A. Ravindran (2016), Effect of stratiform heating on the planetary-scale organization of tropical convection, *J. Atmos. Sci.*, *73*, 371–392, doi:10.1175/JAS-D-15-0178.1.

Derbyshire, S., I. Beau, P. Bechtold, J. Grandpeix, J. Piriou, J. Redelsperger, and P. Soares (2004), Sensitivity of moist convection to environmental humidity, *Q. J. R. Meteorol. Soc.*, *130*(604), 3055–3079.

Dorrestijn, J., D. T. Crommelin, A. P. Siebesma, H. Jonker, and C. Jakob (2015), A stochastic multicloud model inferred from radar data for parameterization of deep convection, *J. Atmos. Sci.*, *72*, 854–869, doi:10.1175/JAS-D-14-0110.1.

Dorrestijn, J., D. T. Crommelin, A. P. Siebesma, H. J. J. Jonker, and F. Selten (2016), Stochastic convection parameterization with Markov chains in an intermediate-complexity GCM, *J. Atmos. Sci.*, *73*(3), 1367–1382, doi:10.1175/JAS-D-15-0244.1.

Flato, G., et al. (2013), Evaluation of climate models, in *Climate Change 2013: The Physical Science Basis. Contribution of Working Group I to the Fifth Assessment Report of the Intergovernmental Panel on Climate Change*, edited by T. Stocker, et al., Cambridge Univ. Press, Cambridge, U. K.

Frenkel, Y., A. Majda, and B. Khouider (2012), Using the stochastic multicloud model to improve tropical convective parameterization: A paradigm example, *J. Atmos. Sci.*, *69*, 1080–1105, doi:10.1175/JAS-D-11-0148.1.

Frenkel, Y., A. J. Majda, and B. Khouider (2013), Stochastic and deterministic multicloud parameterizations for tropical convection, *Clim. Dyn.*, *41*(5-6), 1527–1551, doi:10.1007/s00382-013-1678-z.

Frenkel, Y., A. J. Majda, and S. N. Stechmann (2015), Cloud-radiation feedback and atmosphere-ocean coupling in a stochastic multicloud model, *Dyn. Atmos. Oceans*, *71*, 35–55, doi:10.1016/j.dynatmoce.2015.05.003.

Gillespie, D. (1975), An exact method for numerically simulating the stochastic coalescence process in a cloud, *J. Atmos. Sci.*, *32*, 1977–1989.
Goswami, B. B., B. Khouider, R. Phani, P. Mukhopadhyay, and A. Majda (2016), Improving synoptic and intra-seasonal variability in CFSv2 via stochastic representation of organized convection, *Geophys. Res. Lett.*, *43*, doi:10.1002/2016GL071542.
Gottwald, G. A., K. Peters, and L. Davies (2016), A data-driven method for the stochastic parametrisation of subgrid-scale tropical convective area fraction, *Q. J. R. Meterol. Soc.*, *142*(694), 349–359, doi:10.1002/qj.2655.
Gregory, D., J.-J. Morcrette, C. Jakob, A. C. M. Beljaars, and T. Stockdale (2000), Revision of convection, radiation and cloud schemes in the ECMWF integrated forecasting system, *Q. J. R. Meterol. Soc.*, *126*(566), 1685–1710, doi:10.1002/qj.49712656607.
Hannah, W. M., and E. D. Maloney (2014), The moist static energy budget in NCAR CAM5 hindcasts during DYNAMO, *J. Adv. Model. Earth Syst.*, *6*, 420–440, doi:10.1002/2013MS000272.
Hirons, L. C., P. Inness, F. Vitart, and P. Bechtold (2013a), Understanding advances in the simulation of intraseasonal variability in the ECMWF model. Part I: The representation of the MJO, *Q. J. R. Meterol. Soc.*, *139*(675), 1417–1426, doi:10.1002/qj.2060.
Hirons, L. C., P. Inness, F. Vitart, and P. Bechtold (2013b), Understanding advances in the simulation of intraseasonal variability in the ECMWF model. Part II: The application of process-based diagnostics, *Q. J. R. Meteorol. Soc.*, *139*(675), 1427–1444, doi:10.1002/qj.2059.
Holloway, C., and J. Neelin (2009), Moisture vertical structure, column water vapor, and tropical deep convection, *J. Atmos. Sci.*, *66*(6), 1665–1683, doi:10.1175/2008JAS2806.1.
Holloway, C. E., S. J. Woolnough, and G. M. S. Lister (2012), Precipitation distributions for explicit versus parametrized convection in a large-domain high-resolution tropical case study, *Q. J. R. Meteorol. Soc.*, *138*(668), 1692–1708, doi:10.1002/qj.1903.
Houze, R. (1997), Stratiform precipitation in regions of convection: A meteorological paradox?, *Bull. Am. Meteorol. Soc.*, *78*, 2179–2196.
Huffman, G. J., R. F. Adler, M. M. Morrissey, D. T. Bolvin, S. Curtis, R. Joyce, B. McGavock, and J. Susskind (2001), Global precipitation at one-degree daily resolution from multisatellite observations, *J. Hydrometeorol.*, *2*(1), 36–50.
Jakob, C. (2010), Accelerating progress in global atmospheric model development through improved parameterizations: Challenges, opportunities, and strategies, *Bull. Am. Meteorol. Soc.*, *91*(7), 869–875.
Jakob, C. (2014), Going back to basics, *Nat. Clim. Change*, *4*, 1042–1045, doi:10.1038/nclimate2445.
Jakob, C., and A. Siebesma (2003), A new subcloud model for mass-flux convection schemes: Influence on triggering, updraft properties, and model climate, *Mon. Weather Rev.*, *131*(11), 2765–2778.
Jiang, X., et al. (2015), Vertical structure and physical processes of the Madden-Julian oscillation: Exploring key model physics in climate simulations, *J. Geophys. Res. Atmos.*, *120*, 4718–4748, doi:10.1002/2014JD022375.
Khouider, B., and A. Majda (2008a), Multicloud models for organized tropical convection: Enhanced congestus heating, *J. Atmos. Sci.*, *65*(3), 895–914.
Khouider, B., and A. Majda (2008b), Equatorial convectively coupled waves in a simple multicloud model, *J. Atmos. Sci.*, *65*(11), 3376–3397.
Khouider, B., J. Biello, and A. Majda (2010), A stochastic multicloud model for tropical convection, *Commun. Math. Sci.*, *8*(1), 187–216.
Khouider, B., A. St-Cyr, A. J. Majda, and J. Tribbia (2011), The MJO and convectively coupled waves in a coarse-resolution GCM with a simple multicloud parameterization, *J. Atmos. Sci.*, *68*(2), 240–264, doi:10.1175/2010JAS3443.1.
Kiladis, G. N., M. C. Wheeler, P. T. Haertel, K. H. Straub, and P. E. Roundy (2009), Convectively coupled equatorial waves, *Rev. Geophys.*, *47*, RG2003, doi:10.1029/2008RG000266.
Kim, D., et al. (2009), Application of MJO simulation diagnostics to climate models, *J. Clim.*, *22*(23), 6413–6436.
Kim, D., A. H. Sobel, E. D. Maloney, D. M. Frierson, and I.-S. Kang (2011), A systematic relationship between intraseasonal variability and mean state bias in AGCM simulations, *J. Clim.*, *24*(21), 5506–5520.
Kim, D., A. H. Sobel, A. D. Del Genio, Y. Chen, S. J. Camargo, M.-S. Yao, M. Kelley, and L. Nazarenko (2012), The tropical subseasonal variability simulated in the NASA GISS general circulation model, *J. Clim.*, *25*(13), 4641–4659.
Kinne, S., D. O'Donnel, P. Stier, S. Kloster, K. Zhang, H. Schmidt, S. Rast, M. Giorgetta, T. F. Eck, and B. Stevens (2013), MAC-v1: A new global aerosol climatology for climate studies, *J. Adv. Model. Earth Syst.*, *5*, 704–740, doi:10.1002/jame.20035.
Klingaman, N. P., and S. J. Woolnough (2014), Using a case-study approach to improve the Madden-Julian oscillation in the Hadley Centre model, *Q. J. R. Meteorol. Soc.*, *140*(685), 2491–2505, doi:10.1002/qj.2314.
Klingaman, N. P., et al. (2015), Vertical structure and physical processes of the Madden-Julian oscillation: Linking hindcast fidelity to simulated diabatic heating and moistening, *J. Geophys. Res. Atmos.*, *120*, 4690–4717, doi:10.1002/2014JD022374.
Klingaman, N. P., G. M. Martin, and A. Moise (2016), ASoP (v1.0): A set of methods for analyzing scales of precipitation in general circulation models, *Geosci. Model Dev.*, *10*, 57–83, doi:10.5194/gmd-10-57-2017.
Koster, R. D., et al. (2004), Regions of Strong Coupling Between Soil Moisture and Precipitation, *Science*, *305*(5687), 1138–1140, doi:10.1126/science.1100217.
Kumar, V. V., C. Jakob, A. Protat, C. R. Williams, and P. T. May (2015), Mass-flux characteristics of tropical cumulus clouds from wind profiler observations at Darwin, Australia, *J. Atmos. Sci.*, *72*(5), 1837–1855, doi:10.1175/JAS-D-14-0259.1.
Kumar, V. V., A. Protat, C. Jakob, C. R. Williams, S. Rauniyar, G. L. Stephens, and P. T. May (2016), The estimation of convective mass flux from radar reflectivities, *J. Appl. Meteorol. Clim.*, *55*(5), 1239–1257, doi:10.1175/JAMC-D-15-0193.1.
Liebmann, B., and C. Smith (1996), Description of a complete (inter-polated) OLR dataset, *Bull. Amer. Meteor. Soc.*, *77*, 1275–1277.
Lin, J., and J. Neelin (2000), Influence of a stochastic moist convective parameterization on tropical climate variability, *Geophys. Res. Lett.*, *27*(22), 3691–3694.
Lin, J., and J. Neelin (2003), Toward stochastic deep convective parameterization in general circulation models, *Geophys. Res. Lett.*, *30*(4), 1162, doi:10.1029/2002GL016203.
Lin, J., B. Mapes, M. Zhang, and M. Newman (2004), Stratiform precipitation, vertical heating profiles, and the Madden-Julian oscillation, *J. Atmos. Sci.*, *61*(3), 296–309, doi:10.1175/1520-0469(2004)061 < 0296:SPVHPA>2.0.CO;2.
Majda, A. J., S. N. Stechmann, and B. Khouider (2007), Madden-Julian Oscillation analog and intraseasonal variability in a multicloud model above the equator, *Proc. Natl. Acad. Sci. U. S. A*, *104*(24), 9919–9924, doi:10.1073/pnas.0703572104.
Majda, A. J., B. Khouider, and Y. Frenkel (2015), Effects of rotation and mid-troposphere moisture on organized convection and convectively coupled gravity waves, *Clim. Dyn.*, *44*(3-4), 937–960, doi:10.1007/s00382-014-2222-5.
Matsuno, T. (1966), Quasi-geostrophic motions in the equatorial area, *J. Meteorol. Soc. Jpn.*, *44*(1), 25–43.
Möbis, B., and B. Stevens (2012), Factors controlling the position of the intertropical convergence zone on an aquaplanet, *J. Adv. Model. Earth Syst.*, *4*, M00A04, doi:10.1029/2012MS000199.
Nordeng, T. (1994), Extended versions of the convective parametrization scheme at ECMWF and their impact on the mean and transient activity of the model in the tropics, in *Tech. Memo.*, 206, Eur. Cent. for Medium-Range Weather Forecasts, Reading, U. K.

Peters, K., C. Jakob, L. Davies, B. Khouider, and A. J. Majda (2013), Stochastic behavior of tropical convection in observations and a multicloud model, *J. Atmos. Sci.*, *70*(11), 3556–3575, doi:10.1175/JAS-D-13-031.1.

Peters, O., A. Deluca, A. Corral, J. D. Neelin, and C. E. Holloway (2010), Universality of rain event size distributions, *J. Stat. Mech.*, *11*, P11030.

Pielke, R. A. (2001), Influence of the spatial distribution of vegetation and soils on the prediction of cumulus convective rainfall, *Rev. Geophys.*, *39*(2), 151–177.

Randall, D., et al. (2007), *Climate Models and Their Evaluation*, Cambridge Univ. Press, Cambridge, U. K.

Reick, C. H., T. Raddatz, V. Brovkin, and V. Gayler (2013), Representation of natural and anthropogenic land cover change in MPI-ESM, *J. Adv. Model. Earth Syst.*, *5*, 459–482, doi:10.1002/jame.20022.

Sperber, K. R., and D. Kim (2012), Simplified metrics for the identification of the Madden-Julian oscillation in models, *Atmos. Sci. Let.*, *13*(3), 187–193, doi:10.1002/asl.378.

Stechmann, S. N., and J. D. Neelin (2011), A stochastic model for the transition to strong convection, *J. Atmos. Sci.*, *68*(12), 2955–2970, doi:10.1175/JAS-D-11-028.1.

Stephens, G. L., T. L'Ecuyer, R. Forbes, A. Gettlemen, J.-C. Golaz, A. Bodas-Salcedo, K. Suzuki, P. Gabriel, and J. Haynes (2010), Dreary state of precipitation in global models, *J. Geophys. Res.*, *115*, D24211, doi:10.1029/2010JD014532.

Stevens, B., and S. Bony (2013), What are climate models missing?, *Science*, *340*(6136), 1053–1054, doi:10.1126/science.1237554.

Stevens, B., et al. (2013), Atmospheric component of the MPI-M earth system model: ECHAM6, *J. Adv. Model. Earth Syst.*, *5*, 146–172, doi:10.1002/jame.20015.

Straub, K. H., and G. N. Kiladis (2003), The observed structure of convectively coupled Kelvin waves: Comparison with simple models of coupled wave instability, *J. Atmos. Sci.*, *60*(14), 1655–1668, doi:10.1175/1520-0469(2003)060 < 1655:TOSOCC>2.0.CO;2.

Tan, J., C. Jakob, and T. P. Lane (2015), The consequences of a local approach in statistical models of convection on its large-scale coherence, *J. Geophys. Res. Atmos.*, *120*, 931–944, doi:10.1002/2014JD022680.

Taylor, K., D. Williamson, and F. Zwiers (2000), The sea surface temperature and sea-ice concentration boundary conditions for AMIP II simulations, *PCMDI Rep.*, *60*, 28 pp., Program for Climate Model Diagnosis and Intercomparison, Lawrence Livermore National Laboratory, University of California, Calif.

Teixeira, J., and C. Reynolds (2008), Stochastic nature of physical parameterizations in ensemble prediction: A stochastic convection approach, *Mon. Weather Rev.*, *136*(2), 483–496.

Thayer-Calder, K., and D. A. Randall (2009), The role of convective moistening in the Madden-Julian oscillation, *J. Atmos. Sci.*, *66*(11), 3297–3312.

Thual, S., A. J. Majda, and S. N. Stechmann (2014), A stochastic skeleton model for the MJO, *J. Atmos. Sci.*, *71*(2), 697–715.

Tiedtke, M. (1989), A comprehensive mass flux scheme for cumulus parameterization in large- scale models, *Mon. Weather Rev.*, *117*(8), 1779–1800.

Tseng, W.-L., B.-J. Tsuang, N. S. Keenlyside, H.-H. Hsu, and C.-Y. Tu (2015), Resolving the upper-ocean warm layer improves the simulation of the Madden-Julian oscillation, *Clim. Dyn.*, *44*(5-6), 1487–1503, doi:10.1007/s00382-014-2315-1.

Waliser, D., et al. (2009), MJO simulation diagnostics, *J. Clim.*, *22*(11), 3006–3030, doi:10.1175/2008JCLI2731.1.

Watson, P. A. G., H. M. Christensen, and T. N. Palmer (2015), Does the ECMWF IFS convection parameterization with stochastic physics correctly reproduce relationships between convection and the large-scale state?, *J. Atmos. Sci.*, *72*(1), 236–242, doi:10.1175/JAS-D-14-0252.1.

Wheeler, M., and G. Kiladis (1999), Convectively coupled equatorial waves: Analysis of clouds and temperature in the wavenumber-frequency domain, *J. Atmos. Sci.*, *56*(3), 374–399, doi:10.1175/1520-0469(1999)056 < 0374:CCEWAO>2.0.CO;2.

Wheeler, M., G. N. Kiladis, and P. J. Webster (2000), Large-scale dynamical fields associated with convectively coupled equatorial waves, *J. Atmos. Sci.*, *57*(5), 613–640, doi:10.1175/1520-0469(2000)057 < 0613:LSDFAW>2.0.CO;2.

Wheeler, M. C., and H. H. Hendon (2004), An all-season real-time multivariate MJO index: Development of an index for monitoring and prediction, *Mon. Weather Rev.*, *132*(8), 1917–1932, doi:10.1175/1520-0493(2004)132 < 1917:AARMMI>2.0.CO;2.

Wu, C.-M., and A. Arakawa (2014), A unified representation of deep moist convection in numerical modeling of the atmosphere: Part II, *J. Atmos. Sci.*, *71*(6), 2089–2103.

Yang, D., and A. P. Ingersoll (2013), Triggered convection, gravity waves, and the MJO: A shallow-water model, *J. Atmos. Sci.*, *70*(8), 2476–2486, doi:10.1175/JAS-D-12-0255.1.

Zhang, C. (2005), Madden-Julian oscillation, *Rev. Geophys.*, *43*, RG2003, doi:10.1029/2004RG000158.

Zhang, C., J. Gottschalck, E. D. Maloney, M. W. Moncrieff, F. Vitart, D. E. Waliser, B. Wang, and M. C. Wheeler (2013), Cracking the MJO nut, *Geophys. Res. Lett.*, *40*, 1223–1230, doi:10.1002/grl.50244.

Zhu, H., and H. H. Hendon (2015), Role of large-scale moisture advection for simulation of the MJO with increased entrainment, *Q. J. R. Meterol. Soc.*, *141*(691), 2127–2136, doi:10.1002/qj.2510.